Application of Multi-Dimensional Deconvolution to Enhance Seismic-While-Drilling Data Imaging

Ning Wang[1], Matteo Ravasi[1], Marine Deheuvels[1], and Tariq Alkhalifah[2]

[1]King Abdullah University of Science and Technology
[2]King Abdullah University of Science and Technology (KAUST), Physical Sciences and Engineering Division, Thuwal, Saudi Arabia

April 25, 2025

Abstract

Seismic-while-drilling (SWD) provides a cost-effective solution to sense the subsurface by utilizing the drill-bit noise as a seismic source. However, extracting useful information from SWD recordings remains challenging due to the erratic and unknown nature of the source signature. Thus, we propose a practical workflow for applying multi-dimensional deconvolution (MDD) to SWD data, producing a reflection response from virtual sources to physical receivers at the Earth's surface that is free of surface-related multiples. A key component of the proposed workflow is the estimation of the direct arrival based on the particle swarm optimization algorithm. This technique refines an initial traveltime curve estimate by maximizing the energy of flattened and stacked raw seismic recordings. Moreover, to maintain the computational cost of MDD to a reasonable level, we adopt a strategy commonly used in seismic interferometry whereby auto- and cross-correlation is applied to time segments of the continuous SWD, and the resulting correlograms are stacked together. MDD is then applied using such waveforms as inputs. The proposed methodology is first validated on a range of synthetic data modeled with an acoustic wave equation, demonstrating the improved quality of the retrieved virtual data and images compared to those obtained from standard correlation-based interferometric redatuming. An additional synthetic test using elastic modeling further confirms the robustness of the proposed workflow. Finally, the proposed method is successfully applied to a field dataset. Both the synthetic and field results demonstrate the effectiveness of this workflow, offering a practical and economically viable solution for processing SWD data.

Application of Multi-Dimensional Deconvolution to Enhance Seismic-While-Drilling Data Imaging

N. Wang[1], **M. Ravasi**[1,2], **M. Deheuvels**[1], **T. Alkhalifah**[1]

[1]Earth Science and Engineering Program, Physical Science and Engineering Division, King Abdullah University of Science and Technology (KAUST),Thuwal, 23955-6900, Kingdom of Saudi Arabia
[2]Shearwater GeoServices, London, United Kingdom

Key Points:

- A workflow is developed to apply multi-dimensional deconvolution (MDD) to seismic-while-drilling data, giving virtual reflection responses.
- A direct arrival removal strategy using particle swarm optimization is devised, improving the accuracy of the input wavefields for MDD.
- A segmented correlation strategy is introduced to reduce the cost of MDD, providing stable input for solving the MDD efficiently.

Corresponding author: Ning Wang, `ning.wang.2@kaust.edu.sa`

Abstract

Seismic-while-drilling (SWD) provides a cost-effective solution to sense the subsurface by utilizing the drill-bit noise as a seismic source. However, extracting useful information from SWD recordings remains challenging due to the erratic and unknown nature of the source signature. Thus, we propose a practical workflow for applying multi-dimensional deconvolution (MDD) to SWD data, producing a reflection response from virtual sources to physical receivers at the Earth's surface that is free of surface-related multiples. A key component of the proposed workflow is the estimation of the direct arrival based on the particle swarm optimization algorithm. This technique refines an initial traveltime curve estimate by maximizing the energy of flattened and stacked raw seismic recordings. Moreover, to maintain the computational cost of MDD to a reasonable level, we adopt a strategy commonly used in seismic interferometry whereby auto- and cross-correlation is applied to time segments of the continuous SWD, and the resulting correlograms are stacked together. MDD is then applied using such waveforms as inputs. The proposed methodology is first validated on a range of synthetic data modeled with an acoustic wave equation, demonstrating the improved quality of the retrieved virtual data and images compared to those obtained from standard correlation-based interferometric redatuming. An additional synthetic test using elastic modeling further confirms the robustness of the proposed workflow. Finally, the proposed method is successfully applied to a field dataset. Both the synthetic and field results demonstrate the effectiveness of this workflow, offering a practical and economically viable solution for processing SWD data.

Plain Language Summary

Seismic-while-drilling (SWD) is a method that uses the noise generated by a drill bit as a seismic energy source to image the subsurface. It is cost-effective, but the unpredictable nature of the noise makes it difficult to extract clear seismic signals for accurate imaging. In this study, we develop a novel approach that applies multi-dimensional deconvolution (MDD) to SWD data. This method transforms the noisy recordings into signals as if they came from conventional sources at the Earth's surface, and it removes surface-related multiples. Our workflow includes a new technique to estimate and remove the direct arrivals using an optimization algorithm and introduces a computationally efficient strategy to handle the large volumes of continuous data. Our method was tested on both synthetic and field data. It produced clearer signals and more accurate subsurface images compared to conventional approaches. The technique also proved to be robust and efficient, even when applied to complex geological models and field data. This study provides improved image quality and reduced computational cost for processing SWD data, making it more accessible for subsurface imaging during drilling operations.

1 Introduction

Seismic-while-drilling (SWD) was first proposed by Weatherby (1936) and has recently emerged as a cost-effective solution for subsurface imaging and monitoring due to the fact it eliminates the need for active seismic sources (F. B. Poletto & Miranda, 2022). Unlike conventional vertical seismic profiles (VSP – Hardage (2000)) that use sources on the Earth's surface and record the propagating wavefield within the borehole, SWD relies on the seismic energy naturally generated by the drill bit during drilling and records seismic wavefields by placing sensors on the Earth's surface. Although SWD data typically exhibit a lower signal-to-noise ratio compared to traditional VSP data (F. B. Poletto & Miranda, 2022), this technique presents several advantages. Since SWD does not require the installation of instruments inside a borehole, it reduces the need for drilling interruptions as required by VSP surveys and therefore lowers operational risk. Additionally, it avoids the downtime and costs associated with suspending drilling operations and removing the drill string, which are necessary steps in VSP surveys (Langenkamp, 1994). This allows SWD to provide near-real-time data without interrupting the drilling process. Moreover, by utilizing the continuous seismic energy generated by the drill bit during drilling, SWD can be considered as a form of reverse VSP or drill-bit VSP, enabling seismic data acquisition without the additional cost of deploying dedicated sources. In general, SWD enables efficient, near-real-time data acquisition while avoiding the operational complexity and added cost of deploying downhole sensors. Due to these benefits, SWD has been applied not only in the oil and gas exploration but also in other contexts, including tunnel construction (F. Poletto & Dordolo, 2002) and geothermal exploration (Naville et al., 2000).

The use of drill-bit vibrations as a seismic source has been explored since the 1960s. For instance, Guy (1961) demonstrated that vibrations generated during drilling could be monitored using surface seismometers. Subsequent studies have investigated various applications of drill-bit signals: some researchers used these vibrations to assess the condition of the drill bit itself (Stuart, 1989; Jardine et al., 1990), while others focused on using the signals for subsurface imaging. Katz (1984), for example, developed a method to estimate the drill bit's position by analyzing coherent signals recorded on the surface. Advancements in processing techniques further expanded the potential of SWD. Rector (1989) proposed to auto-correlate the drill-string pilot signal to suppress multiples generated by the drill string. Rocca et al. (1990) explored the use of drill-bit signals for borehole seismic applications by placing pilot sensors on the rig and within the noisy drilling environment. In a field study, Khaled et al. (1996) demonstrated the feasibility of processing SWD data, noting that while the data can be affected by factors such as rock type and drill bit characteristics, it can still produce reliable signals, as shown in their work on the Raudhatain field.

To improve the signal-to-noise ratio of SWD data, researchers often correlate the surface-recorded wavefields with reference pilot signals generated by the drill bit (F. B. Poletto & Miranda, 2022). This approach is conceptually similar to seismic interferometry (SI), a method used to reconstruct the Green's function through cross-correlation of recorded wavefields (Claerbout, 1968; Wapenaar & Fokkema, 2006), which has been successfully applied in various field studies (Campillo & Paul, 2003; Picozzi et al., 2009; de Ridder & Biondi, 2013; Mordret et al., 2015; Galetti et al., 2017). A key difference between dill-bit SWD processing and traditional SI lies in the handling of the source signal. Drill-bit SWD methods typically rely on pilot signals to perform the correlation, while SI does not require any prior knowledge of the source signature. This allows SI to generate virtual sources and reconstruct redatumed surface records directly from the recorded data (Wapenaar & Fokkema, 2006; Schuster, 2009, 2014). The concept of drill-bit SI without pilot signals has also been explored by Miller et al. (1990); Vasconcelos and Snieder (2008a, 2008b), while implementations using pilot signals are presented in studies such as F. Poletto et al. (2010) and Silvestrov et al. (2021). Some other successful field applications further demonstrate the potential of SWD-based methods in both onshore (Miranda et al., 1996; Naville et al., 2004; Bakulin et al., 2020) and offshore environments (F. Poletto et al., 2019; Goertz et al., 2020). These examples highlight the growing interest in SWD as a valuable tool for acquiring additional subsurface information in field drilling projects.

While cross-correlation or single-channel deconvolution-based SI can reconstruct virtual responses and has been used to image the shallow subsurface directly from SWD data (Asgharzadeh et al., 2019), these methods often fail to adequately address surface-related multiples. Moreover, non-ideal illumination conditions can lead to the generation of additional non-physical artifacts in the resulting images. Multi-dimensional deconvolution (MDD) offers a robust alternative solution that can improve the quality of the retrieved Green's function through the deconvolution of the up- and down-going components of the recorded data at a certain datum of interest (Wapenaar et al., 2011). Recent applications of MDD to ocean-bottom data, both on the receiver and source sides, have demonstrated its ability to suppress overburden effects and produce more accurate virtual seismic responses with minimal artifacts (Ravasi et al., 2022; Boiero et al., 2023; Haacke & Poole, 2023; Wang & Ravasi, 2024).

In this study, we propose a novel workflow for multi-dimensional processing and deconvolution of SWD data. The method effectively relocates the seismic source from the drill bit to virtual positions at the Earth's surface, enabling the retrieval of a virtual reflection response that is free from both surface-related multiples and source signature effects. Two key challenges addressed in the proposed workflow are the identification and removal of the direct arrival component from the recorded wavefield, and the application of MDD to long-duration continuous recordings (which can often last several minutes) for each depth point (i.e., source location). To overcome these issues, we develop a data-driven procedure that leverages a global optimization procedure to estimate and remove the direct arrivals. We also propose to solve the normal equations of the MDD problem as this allows us to segment the continuous recordings into smaller time windows, followed by auto- and cross-correlations (which now represents the inputs of the MDD problem). This segmentation and correlation strategy significantly reduces the size of the input wavefields and renders MDD a computationally feasible procedure for SWD data.

The proposed workflow is first validated using synthetic data generated through acoustic modeling using models of increasing structural complexity. Next, to further assess its robustness in field-like conditions, the method is tested on a dataset generated through elastic modeling. The results are compared with those obtained through conventional cross-correlation based redatuming, demonstrating the improved accuracy and reliability of the proposed approach. Finally, the method is applied to a field dataset, and the resulting images reveal structural information that is consistent with the available lithological interpretation from the well cuttings.

2 Theory

2.1 Multi-Dimensional Deconvolution for SWD data

First, let us consider an ocean bottom acquisition geometry, as illustrated in Figure 1a, where sources ($\mathbf{x}_S$) are located just below the sea surface, while both receivers ($\mathbf{x}_R$) and virtual sources ($\mathbf{x}'_R$) are positioned at the sea floor level Λ_R. In this setup, the down-going ($d^+(\mathbf{x}'_R, \mathbf{x}_S)$) and up-going ($d^-(\mathbf{x}_R, \mathbf{x}_S)$) wavefields, propagating from a source ($\mathbf{x}_S$) to receivers ($\mathbf{x}_R$) and virtual sources ($\mathbf{x}'_R$), are related to the local reflection response $R(\mathbf{x}_R, \mathbf{x}'_R)$ via the following multidimensional convolution integral:

$$d^-(\mathbf{x}_R, \mathbf{x}_S) = \int_{\Lambda_R} R(\mathbf{x}_R, \mathbf{x}'_R) d^+(\mathbf{x}'_R, \mathbf{x}_S) d\mathbf{x}'_R, \tag{1}$$

where superscripts (-) and (+) denote the up-going and down-going components, respectively. Here, the local reflection response R represents the seismic response in a medium that is equivalent to the original medium below the datum Λ_R and homogeneous above (i.e., free from interactions with the overburden). The process of solving for R by inverting equation 1 is usually referred to as MDD (Wapenaar et al., 2011; Ravasi et al., 2022).

Since applying receiver-side MDD requires having access to a dense receiver array, which may not always be available in seabed acquisition settings, source-side MDD has been recently proposed as an alternative approach to estimate the local reflection response between source locations (Λ_S) (Vidal & Wapenaar, 2014; Boiero et al., 2023). In this approach, the role of the sources and receivers in Figure 1a is swapped: mirrored receivers are treated as sources, generating the wavefields shown in Figure 1b (Wang & Ravasi, 2023). Based on this reciprocal ocean bottom acquisition geometry, source-side MDD

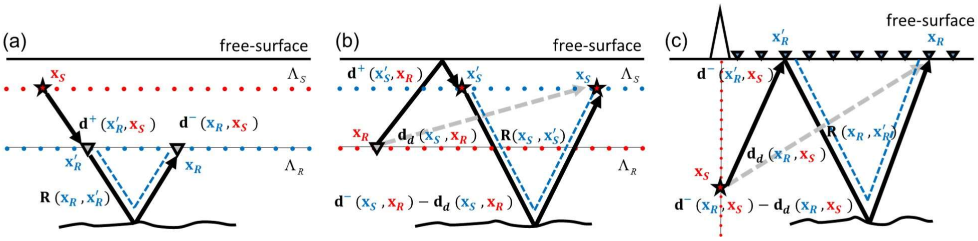

Figure 1. Schematic representation of the wavefields involved in (a) the receiver-side MDD geometry, (b) the source-side MDD geometry, and (c) the SWD geometry. The dashed grey line represents the direct arrival, the dashed blue line represents the reflection response, and the solid black line represents the recorded wavefield.

can be expressed as:

$$\widetilde{d}^-(\mathbf{x}_S, \mathbf{x}_R) = \int_{\Lambda_S} R(\mathbf{x}_S, \mathbf{x}'_S) d^+(\mathbf{x}'_S, \mathbf{x}_R) d\mathbf{x}'_S, \tag{2}$$

where $\mathbf{x}'_S$ represents the virtual receivers, while the superscript $\widetilde{}$ indicates that the wavefield $d^-(\mathbf{x}_S, \mathbf{x}_R)$ is free of the direct arrival component $d_d(\mathbf{x}_S, \mathbf{x}_R)$: $\widetilde{d}^-(\mathbf{x}_S, \mathbf{x}_R) = d^-(\mathbf{x}_S, \mathbf{x}_R) - d_d(\mathbf{x}_S, \mathbf{x}_R)$. Note that the spatial integral is now performed over the source carpet, which is usually regularly and densely sampled.

By moving the virtual receiver array in the reciprocal ocean bottom geometry (blue dots in Figure 1b) to the location of the free surface, the source-side MDD geometry aligns with that of an SWD experiment, as shown in Figure 1c. In this case, the sources located in the well can be interpreted as virtual sources mirrored by the free surface. As a result, only the up-going wavefield on the source side is considered in the MDD formulation. As illustrated in Figure 1c, the up-going wavefield on the source side ($d^-(\mathbf{x}'_R, \mathbf{x}_S)$) is convolved with the local reflection response ($R(\mathbf{x}_R, \mathbf{x}'_R)$) to generate the total up-going wavefield without the direct arrival ($d^-(\mathbf{x}_R, \mathbf{x}_S) - d_d(\mathbf{x}_R, \mathbf{x}_S)$):

$$d^-(\mathbf{x}_R, \mathbf{x}_S) - d_d(\mathbf{x}_R, \mathbf{x}_S) = \int_{\Lambda_R} R(\mathbf{x}_R, \mathbf{x}'_R) d^-(\mathbf{x}'_R, \mathbf{x}_S) d\mathbf{x}_R. \tag{3}$$

By solving equation 3 for R, sources originally located within the well can be effectively relocated to the same position of the surface receivers. The retrieved local reflection response R is moreover free from surface-related multiples and source signature effects.

In practice, equation 3 is discretized over both the time and spatial axes and represented in the following compact matrix-vector notation:

$$\mathbf{d}^- - \mathbf{d}_d = \mathbf{D}^- \mathbf{r}, \tag{4}$$

where $\mathbf{r}$ represents the reflection response to be recovered, and $\mathbf{D}^-$ is a multi-dimensional convolutional operator whose integral kernels contains an ensemble of continuous recordings $d^-(\mathbf{x}'_R, \mathbf{x}_S)$, one for each source location in the wellbore.

2.2 Pre-processing workflow of SWD data

To apply equation 4 to SWD data, the recorded wavefield must first be decomposed into up- and down-going components on the source side, and the direct arrival must be removed from the up-going wavefield. The proposed pre-processing workflow therefore consists of two main steps: i) removing the down-going wavefield from the source side, and ii) removing the direct arrivals from the up-going wavefield. The first step is typically achieved by transforming each common-receiver gather (CRG) into the frequency-wavenumber (f-k) domain and separating wavefield components based on their apparent slowness, which is a standard technique in VSP data processing (Seeman & Horowicz, 1983). However, this step is not straightforward in practice due to the unknown start time of the source wavelet. In this paper, we assume the first step is feasible in the first two synthetic examples presented in the next section, in order to establish a benchmark. In the third test presented in the Synthetic Examples section, we investigate the implications of skipping this step by presenting results without this pre-processing, to evaluate the robustness of the MDD approach under more realistic, field-like conditions. The second step addresses the removal of the direct arrival from the up-going wavefield. Unlike in traditional active-seismic experiments, the SWD source signature is random and usually unknown, unless a sensor is deployed near the drill bit. As a result, conventional direct arrival removal methods are not applicable.

Instead, to accurately identify and remove the direct arrival component from raw SWD data, we employ a global optimization method – specifically, particle swarm optimization (PSO – Kennedy and Eberhart (1995)), to obtain an estimate of the direct traveltime curve $\tau(x_r)$ from the source in the well-bore to the surface receivers, which optimally aligns and stacks the continuous recording along the receiver aperture. The procedure begins by flattening a continuous recording (i.e., a common-shot like gather – CSG) using an initial traveltime estimate, $\tau_0(x_r)$, which can be analytically computed from a constant velocity model or numerically computed from a smoothly varying velocity model. This initial estimate is refined within the PSO framework by applying small, randomized time shifts to each trace and maximizing the squared L_2 norm of the stacked flattened CSG – or equivalently, minimizing its negative squared L_2 norm. This formulation is based on the fact that the direct arrival typically exhibits the highest amplitude in the CSG. The optimization process aims to determine the true direct traveltime curve by ensuring that the CSG flattened using the refined traveltime of the direct arrival presents events associated with the direct component of the wavefield as flat as possible, thereby maximizing the amplitude of the stacked wavefield. To ensure physically reasonable and smooth variations in the estimated traveltime curve, a regularization term is added to constrain the time-shift differences between adjacent traces ($\text{diff}(\tau(x_r))$), limiting abrupt changes and promoting lateral continuity in the final traveltime estimate. The overall optimization problem is therefore formulated through the following objective function:

$$\arg\min_{\tau(x_r)} -||\sum_{x_r} d(t-\tau(x_r), x_r)||_2^2 + \alpha \,\|\text{diff}(\tau(x_r))\|_2^2\,, \tag{5}$$

where α is a regularization parameter.

PSO is a population-based stochastic algorithm designed to solve high-dimensional, non-convex optimization problems. Inspired by the collective behavior of bird flocks searching for food, PSO explores the solution space through a swarm of candidate solutions known as particles. In this study, each particle represents a vector of traveltime shifts applied to the different traces within a CSG. These shifts are iteratively adjusted to minimize the objective function defined in equation 5. During each iteration, the position and velocity of each particle are updated based on a combination of its personal best solution and the global best solution found by the swarm. The particle's velocity determines the step size and direction of movement within the search space, while its position corresponds to a candidate solution. The updated position (traveltime shift) for the i-th particle at iteration $k+1$, is given by:

$$\tau_i^{(k+1)}(x_r) = \tau_i^{(k)}(x_r) + v_i^{(k+1)}(x_r), \tag{6}$$

where i denotes the particle index, and k represents the iteration number. The term $\tau_i^{(k)}(x_r)$ represents the current position of particle i, which in this context represents a set of traveltime shifts applied to the traces in a CSG. The term $v_i^{(k)}(x_r)$ is the corresponding current velocity (or adjustment of position), dictating the direction and magnitude of change in the solution space. The updated position $\tau_i^{(k+1)}(x_r)$ represents the new set of traveltime shifts for the next iteration. In this study, the dimensionality of each particle equals the number of traces in a CSG, as each trace requires an independent shift to be optimized.

The particle velocity controls how quickly particles explores the solution space. A high velocity enhances exploration, allowing particles to search a broader range of candidate solutions, though this may increase the risk of overshooting the optimal solution. In contrast, a low velocity promotes local exploitation, enabling finer adjustments around promising areas but with a higher likelihood of getting trapped in local optima. The velocity update is computed using the following equation:

$$v_i^{(k+1)}(x_r) = \omega v_i^{(k)}(x_r) + \phi_p r_p (p_i^{(k)}(x_r) - \tau_i^{(k)}(x_r)) + \phi_g r_g (g^{(k)}(x_r) - \tau_i^{(k)}(x_r)). \tag{7}$$

This expression consists of three main components. The inertia term, $\omega v_i^{(k)}(x_r)$, represents a weighted contribution of the particle's previous velocity, maintaining momentum. The cognitive term, $\phi_p r_p (p_i^{(k)}(x_r) - \tau_i^{(k)}(x_r))$, attracts the particle toward its own best-known position, encouraging self-guided refinement. The social term, $\phi_g r_g (g^{(k)}(x_r) - \tau_i^{(k)}(x_r))$, encourages movement toward the globally optimal solution found by the swarm, promoting collective intelligence. Here, the parameter ω is the inertia weight, which balances exploration and exploitation: a larger ω enhances the global search ability, while a smaller ω promotes faster convergence. The variables r_p and r_g are uniformly distributed random numbers between 0 and 1, introducing stochastic variability into the search process. The coefficients ϕ_p and ϕ_g determine the influence of personal versus global best positions, respectively. Finally, the variable $p_i^{(k)}(x_r)$ denotes the best-known position of particle i, while $g^{(k)}(x_r)$ represents the best position found by the entire swarm up to iteration k.

Once the optimal time shifts are determined, each CSG is flattened using the final traveltime curve. This process flattens the continuous train of direct arrivals, which typically corresponds with the events of strongest amplitude, while other seismic events appear curved. As a result, when the flattened CSG is stacked into a single trace, the direct arrival constructively reinforces due to its consistent polarity, whereas other events, containing both positive and negative amplitudes, tend to cancel out. The resulting stacked trace, which predominantly represents the direct arrival, is then redistributed across all receiver positions and each trace is shifted back to its original travel time, yielding an estimate of the direct arrival. Finally, the estimated direct arrival is adaptively subtracted from the up-going wavefield, resulting in the up-going component without the direct arrivals.

2.3 MDD implementation

The local reflection response in equation 3 ideally requires the full up-going wavefield and its counterpart with the direct arrival removed, denoted as $\mathbf{d}^-$ and $\mathbf{d}^- - \mathbf{d}_d$, respectively. However, in practice, due to the slowly moving drill-bit, one can safely assume that the SWD recording for each 'stationary' source location in the wellbore can last up to several minutes; using several or such recordings to form the MDD equations can therefore results in a prohibitively high memory consumption.

To circumvent this, we propose here to solve the normal equations of the MDD problem:

$$\mathbf{D}^H(\mathbf{d}^- - \mathbf{d}_d) = (\mathbf{D}^H \mathbf{D}^-)\mathbf{r}. \tag{8}$$

However, under the assumption that the auto- and cross-correlation of $\mathbf{d}^-$ and $\mathbf{d}^- - \mathbf{d}_d$ have a decorrelation length in the order of some seconds, much shorter time recordings can be effectively used as input to the MDD process. Moreover, as commonly done in

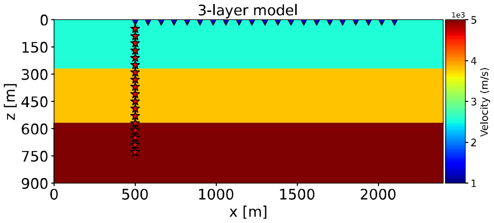

Figure 2. Three-layer velocity model. Red stars represent sources positions within a well, and blue triangles represent surface receivers locations.

standard seismic interferometric process (Zhang et al., 2020), the continuous processed wavefields ($\mathbf{d}^-$ and $\mathbf{d}^- - \mathbf{d}_d$) are divided into time segments with a duration of only a few seconds ($\mathbf{d}_i^-$ and $\mathbf{d}_i^- - \mathbf{d}_{d,i}$), where i denotes the segment index. Auto- and cross-correlation are then performed for each segment individually and the resulting correlated wavefields are stacked together. In other words, this corresponds to applying the adjoint of the modeling operator with the up-going wavefield ($\mathbf{D}_i^H$) to both sides of equation 3 independently for each segment and stacking the results from all segments:

$$\sum_i \mathbf{D}_i^H(\mathbf{d}_i^- - \mathbf{d}_{d,i}) = \sum_i (\mathbf{D}_i^H \mathbf{D}_i^-)\mathbf{r}. \tag{9}$$

This approach produces an approximate representation of the wavefields $\mathbf{D}^H(\mathbf{d}^- - \mathbf{d}_d)$ and $\mathbf{D}^H\mathbf{D}^-$. To our knowledge, this strategy, although very popular in the field of seismic interferometry, it has not previously been applied within the context of MDD. Incorporating this step significantly improves the clarity of the input data for the normal MDD equation (equation 9) compared to the original SWD MDD equation 4, and ultimately facilitates a more stable and easier MDD process. Additionally, the segmentation approach enables MDD to be performed on a much smaller dataset, significantly reducing both memory and computational costs.

3 Synthetic examples

To demonstrate the effectiveness of the proposed method, we first apply it to a set of synthetic data sets generated using acoustic modeling. This provides a controlled environment to validate each step of the workflow. We then apply the method to a data set modeled with elastic wave propagation to mimic a more realistic setting closer to that expected in field conditions.

3.1 Three-layer model

To clearly illustrate the pre-processing workflow, we begin with a simple three-layer acoustic model (Figure 2). The acquisition setup includes 401 surface receivers spaced every 4 m between 500 and 2100 m, represented by blue triangles in Figure 2, and 351 sources placed along a vertical borehole from 50 to 750 m at 2 m intervals, represented by red stars. To simulate a realistic SWD data set, seismic data are first modeled using an impulsive source with free-surface effects included. The resulting data are then convolved with a source signature composed of 3 minutes of white Gaussian noise, mimicking the continuous nature of drill-bit energy. A 1.5 s close-up of a representative CSG from a source depth of 150 m is shown in Figure 3a.

To apply the proposed method, we first arrange the data set into the CRG for processing as shown in Figure 3b. Wavefield separation is then performed in the f-k domain

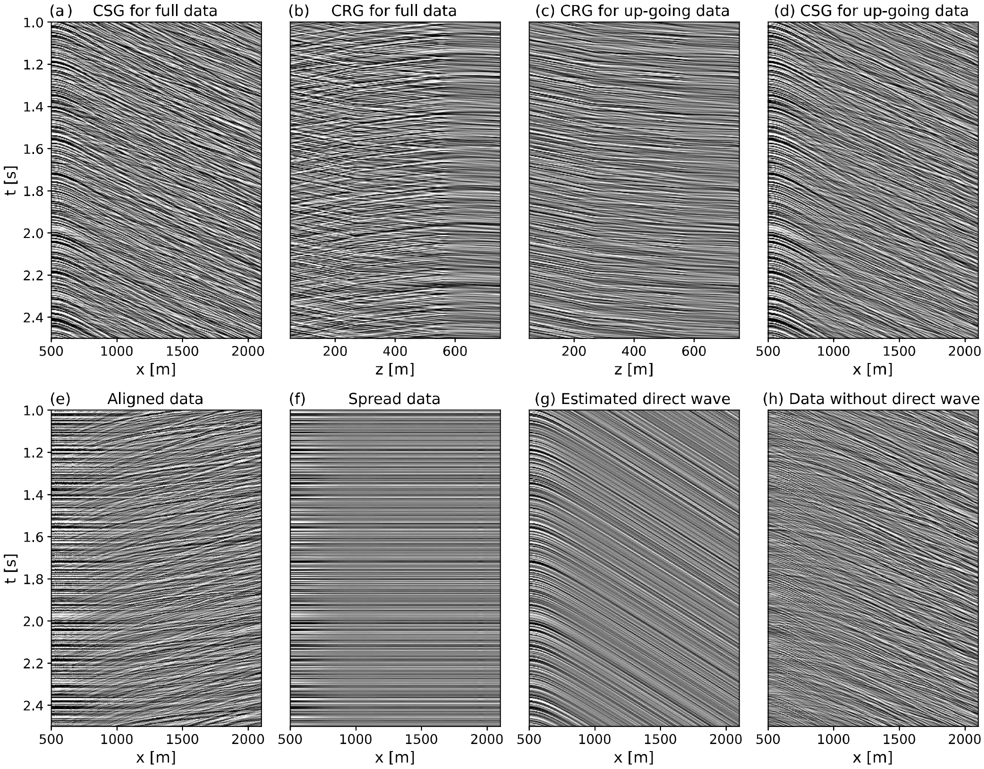

Figure 3. (a) CSG of the full data, (b) CRG of the full data, (c) CRG of the the up-going wavefield, (d) CSG of the the up-going wavefield, (e) aligned wavefield using the optimized time shift, (f) stacked direct arrival trace spread across the entire receiver array, (g) estimated direct arrival wavefield, (h) up-going wavefield after direct arrival removal via adaptive subtraction.

based on slowness, removing the down-going component. The resulting up-going component is shown in CRG and CSG formats in Figures 3c and 3d, respectively. Next, PSO-based alignment method is applied to each up-going CSG to flatten the direct arrival (Figure 3e). The aligned wavefield is then stacked and re-distributed across all traces to suppress events other than direct arrival, producing the wavefield shown in Figure 3f. Shifting this re-distributed trace back to its original traveltime positions yields the estimated direct arrival (Figure 3g). Finally, the estimated direct arrival is removed from the up-going wavefield using adaptive subtraction, yielding an approximation of the coda of the up-going wavefield (i.e., up-going wavefield deprived of the contribution of the direct arrivals) as shown in Figure 3h. To manage the large volume of continuous data, the 3-minute recording is divided into 4-second segments. For each segment, cross-correlation is performed between the up-going wavefield and the up-going wavefield with the direct arrival removed, while auto-correlation is applied to the original up-going wavefield. The resulting correlegrams from all of the different segments are then summed together to produce the input wavefields for normal equations of the MDD process, as shown in Figures 4a and 4b.

Subsequently, the local reflection response is obtained through MDD (Figure 4d); note how this free of surface-relate multiples and source signature effects. For comparison, the wavefield obtained using conventional cross-correlation is also presented in Figure 4e. This result is also free from source signature effects, however, several free-surface

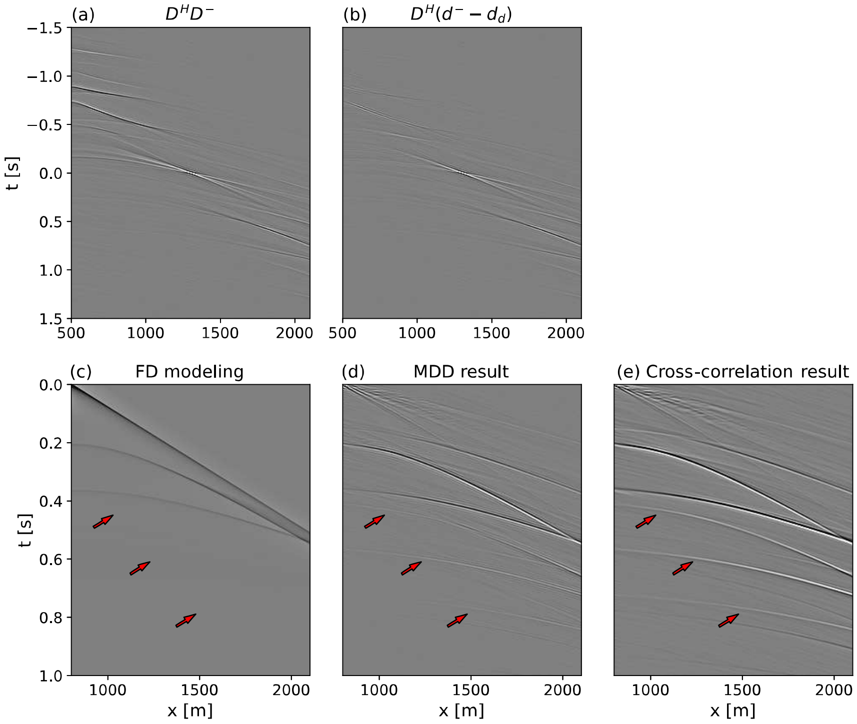

Figure 4. (a) Auto-correlation of the up-going wavefield, (b) cross-correlation between the up-going wavefield and the up-going wavefield with the direct arrival removed. Reconstructed wavefields using (c) FD modeling, (d) MDD, and (e) cross-correlation.

multiples are still present (red arrows in Figure 4e). Additionally, a reference solution is computed using finite-difference (FD) modeling without free-surface effects, employing an impulsive source and positioning both sources and receivers at the Earth's surface (a shot gather from it is shown in Figure 4c). It is important to note that both the MDD and cross-correlation results represent single-sided wavefields, propagating from the well towards increasing positive offsets. This asymmetry arises from the geometry of the SWD acquisition (Figure 1c), as sources are located in the well and energy propagates away from it. As a result, the local reflection response lacks contributions from virtual sources to receivers that lie on either side of the wellbore. Therefore, here we only present the resulting wavefield arranged as CSGs with a virtual source positioned at x = 800 m and receivers placed on the far side of the well, covering the range from x = 800 to 2100 m. Compared to the reference result, the MDD output successfully reconstructs both primary reflection responses, while the cross-correlation result contains noticeable artifacts, as indicated by the red arrows in Figures 4c–4e.

To further assess imaging quality, the wavefields obtained from all three methods are imaged using pre-stack Kirchhoff depth migration. As shown in Figure 5, image produced from MDD (Figure 5b) closely matches the reference image derived from FD modeling (Figure 5a). It successfully recovers both reflectors and effectively suppresses multiple-related artifacts, which remain visible in the image generated from the cross-correlation result (Figure 5c). These results validate the effectiveness of the proposed method in accurately recovering the reflection response while handling both the unknown source signature and surface-related multiples.

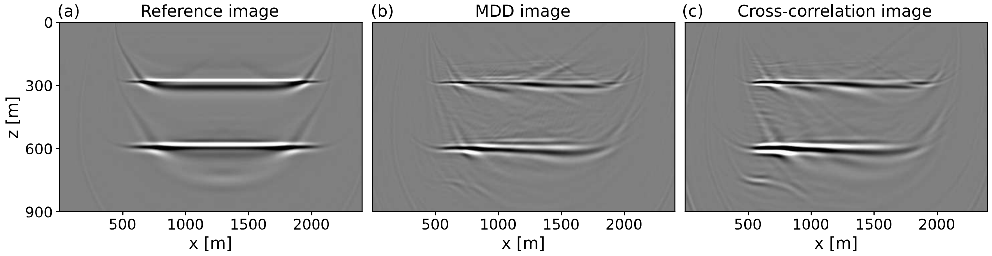

Figure 5. Imaging results obtained from data modeled using (a) FD modeling, (b) MDD, and (c) cross-correlation.

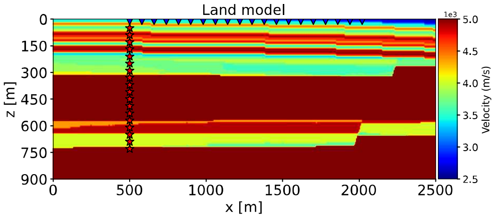

Figure 6. Land velocity model. Red stars represent sources positions within a well, and blue triangles represent surface receivers locations.

3.2 Land model

Next, we apply the proposed method to a more geologically complex land model (Figure 6), adapted from the SEAM Arid model (Oristaglio, 2015). This model features numerous faults and high-contrast layers, providing a more realistic test for the proposed workflow. A vertical well is placed at x = 500 m, where 351 sources are placed along the borehole at 2 m intervals from depths of 50 to 750 m (shown as red stars in Figure 6). On the surface, 401 receivers are deployed with 4 m spacing, spanning from 500 to 2100 m (represented by the blue triangles). Following the same procedure described in the previous example, seismic data are first simulated using an impulsive source with free-surface effects included and then convolved with a source signature consisting of 3-minutes white Gaussian noise.

The pre-processing workflow for this example is also the same as the one described for the three-layer model. We begin by removing the source-side down-going component of the wavefield; this is followed by the PSO-based alignment process to estimate and subtract the direct arrival. Next, the processed three-minute recording is divided into four-second segments. For each segment, correlations are performed and then summed to generate the input wavefields required to solve the normal equations of the MDD problem, as shown in Figure 7a and 7b. Due to the complex subsurface structure, the wavefields are clearly more intricate than those from the simple three-layer model. The local reflection response obtained through MDD using the processed data and the cross-correlation result are shown in Figure 7d and 7e, respectively. Compared to the reference reflection response without free surface effect produced by FD modeling with co-located sources and receivers on the surface (Figure 7c), both MDD and cross-correlation results contain artifacts, with the cross-correlation result showing more pronounced ringing as indicated by the red arrow. Subsequently, Kirchhoff migration is applied to the three different wavefields. Both the MDD (Figure 8b) and the cross-correlation (Figure 8c) images capture the main subsurface structures and are in good agreement with the

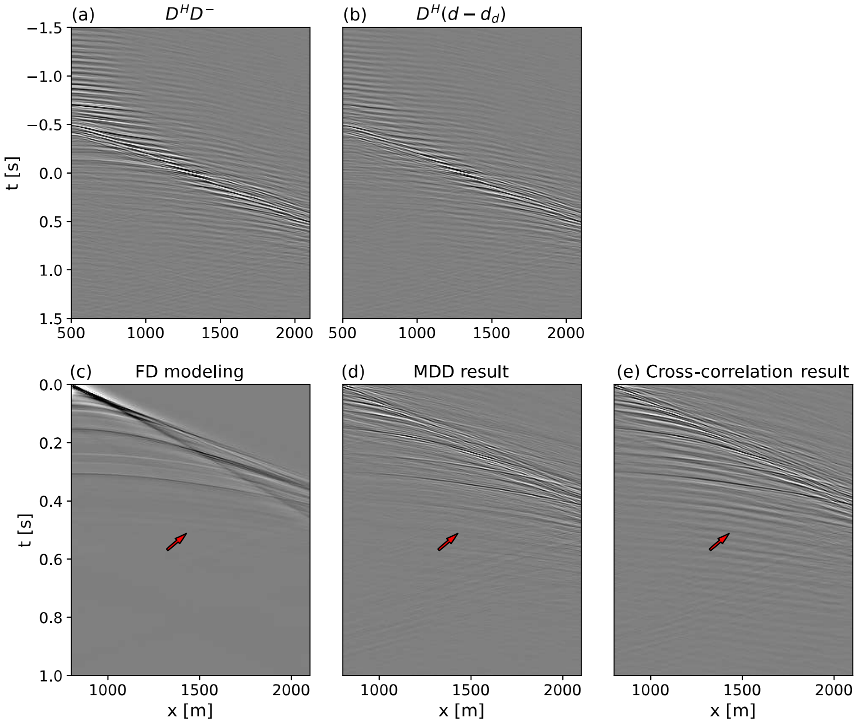

Figure 7. (a) Auto-correlation of the up-going wavefield, (b) cross-correlation between the up-going wavefield and the up-going wavefield with the direct arrival removed. Reconstructed wavefields using (c) FD modeling, (d) MDD, and (e) cross-correlation.

reference image from FD modeling (Figure 8a). However, the cross-correlation image displays more noticeable artifacts, again highlighted by red arrows. Moreover, some of the far-offset structures within the yellow squares (Figure 8), exhibit reduced illumination compared to the near-offset region. This limitation arises from insufficient receiver coverage. Similarly, deeper subsurface features, marked by the blue squares, are poorly resolved due to limited contribution from deeper sources, which are essential for illuminating these areas effectively. It is important to note that these limitations are not a shortcoming of the proposed method, rather inherent to the SWD acquisition geometry. Despite these challenges, the results demonstrate the ability of the proposed method to suppress artifacts and improve image quality in complex geological environments. Compared to the conventional cross-correlation approach, which produces noisier results with more visible artifacts, the MDD-based method offers clearer, more accurate images.

3.3 Three-layer model by elastic modeling

In real-life scenarios, the wavefield generated by the drilling bit is more complex due to the elastic nature of the subsurface. To evaluate the practicality of the proposed method under more realistic conditions, we apply it to synthetic data generated using elastic wavefield modeling.

Another key challenge we face in real data is the application of wavefield separation on the source side. In the previous tests, each source shared the same 3-minute random noise signature, allowing for coherent wavefield construction in the CRG domain. However, in practice, the drill-bit-generated noise varies for each source, making the recorded

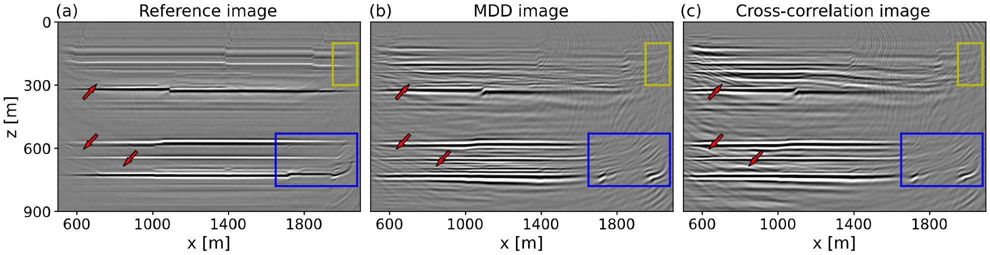

Figure 8. Imaging results obtained by (a) FD modeling, (b) MDD and (c) cross-correlation.

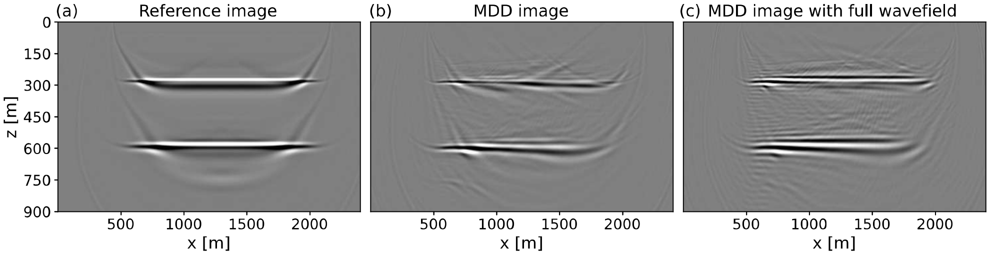

Figure 9. Imaging results obtained from data modeled using (a) FD modeling, (b) MDD with only up-going component on the source side, and (c) MDD with full wavefield.

wavefield incoherent from trace to trace. As a result, wavefield separation using slowness-based methods becomes infeasible for field data. While ideal in theory, wavefield separation is not practical for field scenarios.

Fortunately, a previous example shows that the down-going component of the wavefield is typically much weaker than the up-going wavefield, making the full wavefield (Figure 3a) and up-going wavefield (Figure 3d) looks pretty much similar. Thus, omitting this step in the processing workflow might have a negligible impact on the final result, as demonstrated in Figure 9c, which accurately depicts the two main layers seen in the reference image (Figure 9a) accurately and closely matches the MDD imaging result obtained using only the up-going component on the source side (Figure 9b).

Next, we present a test using the same three-layer model and acquisition geometry shown in Figure 2, but simulated using elastic modeling. Here, each source is assigned a unique 3-minute white Gaussian noise signal to reflect the variability observed in real drill-bit operations, while free-surface effects are also included in the modeling. A representative CSG is shown in Figure 10a. Compared to its acoustic counterpart (Figure 3a), the elastic data set contains an additional prominent component: the ground roll, which dominates the wavefield with strong energy. Figure 10b presents a CRG constructed using different source signatures. In contrast to the CRG with identical source signatures in Figure 3b, the wavefield appears incoherent and noisy, preventing successful wavefield separation. To suppress the ground roll, every CSG is transformed into the f-k domain, where components are separated based on their apparent slopes. The resulting wavefield without ground roll arranged as CSG is shown in Figure 10c. This wavefield more closely resembles the acoustic wavefield in Figure 3d, though it contains slightly more converted wave energy and some residual ground roll, as indicated by the red arrows in Figure 10c. As expected, the corresponding CRG (Figure 10d) remains noisy due to the incoherent source signatures. Subsequently, each CSG is flattened using the PSO-based alignment method, as shown in Figure 10e. The aligned wavefield is then stacked and spread across

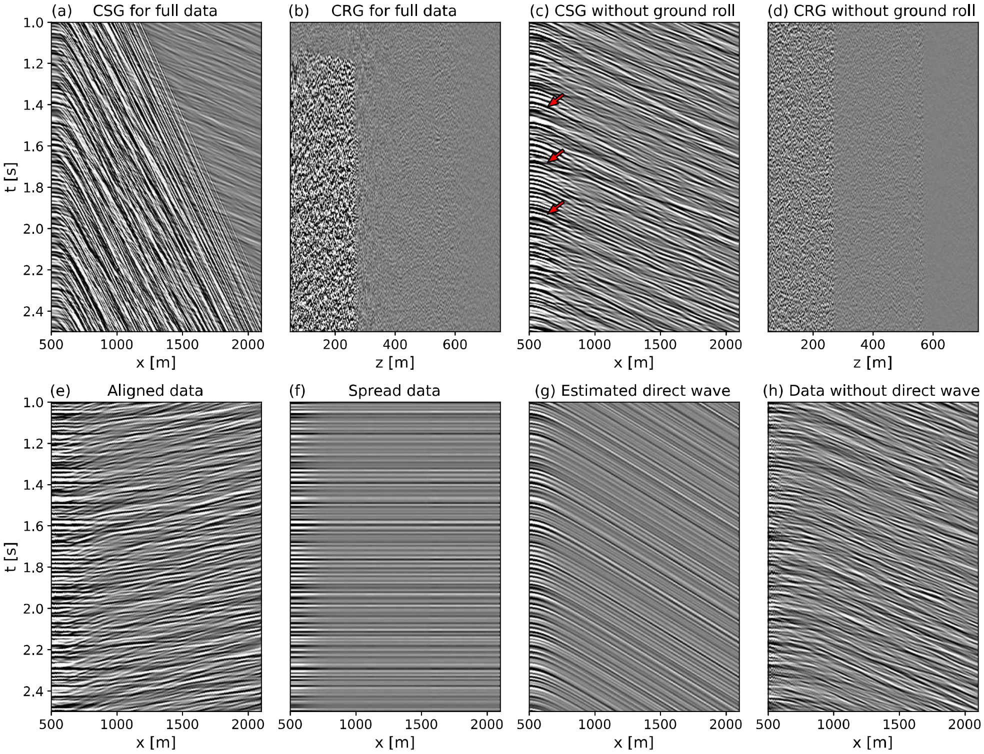

Figure 10. (a) CSG of the full data, (b) CRG of the full data, (c) CSG without ground roll, (d) CSG without ground roll, (e) aligned wavefield using the optimized time shift, (f) spread wavefield, (g) estimated direct arrival wavefield, (h) wavefield without the direct arrival

all traces (Figure 10f), followed by shifting the result back to reconstruct the estimated direct arrival (Figure 10g). The total wavefield without the direct arrival is then obtained by adaptive subtraction as shown in Figure 10h. Compared to the acoustic case (Figure 3h), the elastic result contains more residual artifacts, primarily due to the influence of ground roll. In this example, a simple filtering approach is used to suppress the ground roll, which yields an acceptable result but could be further improved using more advanced suppression techniques. Next, the segmentation method is applied to the 3-minute recordings, which is followed by correlation and summation to produce the final input wavefield for normal MDD, as shown in Figures 11a and 11b. As expected, these inputs contain more noise than those obtained from acoustic modeling.

The local reflection response is then retrieved using MDD applied to the processed elastic data, as shown in Figure 11d, and cross-correlation result is shown in Figure 11e. Both of the MDD and cross-correlation results successfully recover two key reflections while showing additional artifacts caused by the imperfect removal of the ground roll as indicated by yellow arrows, which is non-present for the acoustic MDD result as shown in Figures 11c. Additionally, the cross-correlation result contains free-surface related artifacts than the MDD result as indicated by the red arrows in Figure 11e.

Finally, the reconstructed wavefields are used to carry out Kirchhoff migration, producing images shown in Figure 12b and Figure 12c. For reference, the migration result from the acoustic MDD case is also included (Figure 12a). The image produced from the elastic MDD wavefield matches quite well that of the acoustic reference MDD wavefield,

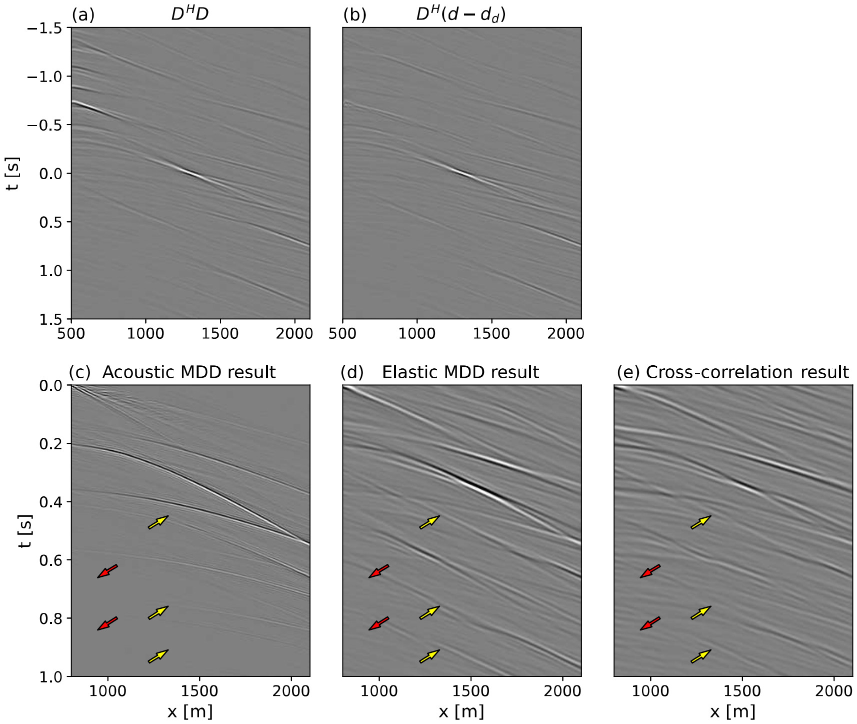

Figure 11. (a) Auto-correlation of the wavefield without ground roll, (b) cross-correlation between the wavefield without ground roll and the wavefield with both the ground roll and direct arrival removed. Reconstructed wavefields using (c) MDD by acoustic modeling, (d) MDD, and (e) cross-correlation.

describing the two layers correctly, however, with some artifacts remaining as marked by the yellow arrow in Figure 12b. As observed in previous examples, the cross-correlation result again exhibits more artifacts than the MDD counterpart, particularly at far offsets and within the second layer, which is poorly imaged as indicated by the red arrow in Figure 12c.

This example highlights two key distinctions relative to the acoustic case: first, ground roll is present due to elastic wave propagation and must be suppressed; second, wavefield separation on the source side was omitted to mimic the conditions of a realistic SWD experiment, where the source signature varies across locations, and yet we obtained good resultds. If more advanced techniques were employed to attenuate ground roll or even converted wave energy, the final results could be further improved. Overall, these results demonstrate the robustness of the proposed method when applied to realistic data sets, even in the presence of down-going wavefield components on the source side. This supports its applicability to field data.

4 Field example

Finally, the proposed method is applied to a field data set acquired at a site located at King Abdullah University of Science and Technology in Saudi Arabia. As shown in Figure 13a, a pilot well (marked by the green triangle) was drilled to a depth of 392 m for monitoring purposes. A total of 89 STRYDE nodes were deployed along a 176-meter-

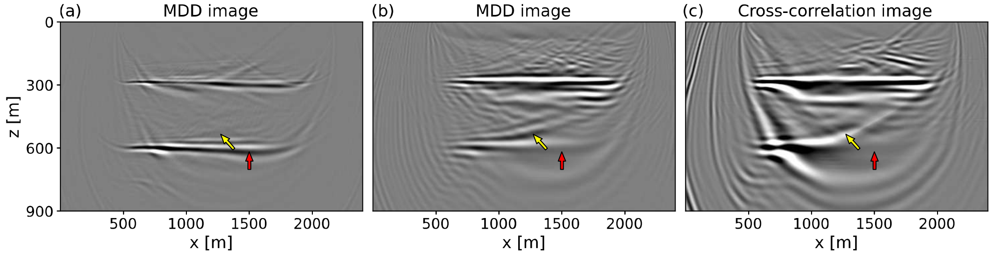

Figure 12. Imaging results obtained by (a) MDD by acoustic modeling, (b) MDD and (c) cross-correlation.

long 2D surface line (shown as the red solid line in Figure 13a), with approximately 2-meter spacing between receivers. These nodes (shown as in Figure 13b) recorded the vertical component of the particle acceleration vector continuously over the course of the drilling operation. According to the drilling report and the STRYDE acquisition schedule shown in Figure 13c, 115 effective SWD source locations were selected for processing, each comprising 8 minutes of continuous recording.

The field data processing flow begins with the application of a band-pass (BP) filter to the original SWD recordings (Figure 14a), removing frequencies below 5 Hz and above 40 Hz. This step attenuates low-frequency ambient noise and high-frequency interference, resulting in a cleaner wavefield, as shown in Figure 14b. When this filtered data is arranged in a CRG configuration, it remains incoherent and noisy (Figure 14c), confirming the earlier observation that wavefield separation on the source side is not feasible for SWD raw data due to inconsistent source signatures. To further suppress coherent surface noise generated by the drilling rig, the filtered data are transformed into the f-k domain and masked, leading to a cleaner wavefield as shown in Figure 14d. Following this step, each CSG is aligned using the PSO-based method (Figure 14e). The aligned wavefield is stacked and redistributed across all traces (Figure 14f), followed by time-shifting to reconstruct the estimated direct arrival (Figure 14g). The estimated direct arrival is then adaptively subtracted, yielding the wavefield without the direct component, as shown in Figure 14h. As in the synthetic examples, the 8-minute processed data sets are divided into 4-second segments. Each segment is correlated and then summed to produce the input wavefields for solving the normal MDD equation, as shown in as shown in Figures 15a and 15b. The final reflection response retrieved through MDD is presented in Figure 15c.

Since the nodes acquired data for only 10 hours a day during the drilling campaign (aside from a nearly month-long pause in the middle of the campaign), the source distribution is irregular, as indicated by the red stars in Figure 16a. The final imaging result is obtained by migrating the reflection response retrieved through MDD using Kirchhoff depth migration. The initial velocity model used for migration (Figure 16a) was derived from a previously acquired active seismic survey. The resulting image, presented in Figure 16b, reveals the presence of four key reflectors at depths of approximately 5, 17, 53, and 126 m. To validate the imaging results, a comparison is made with the lithological profile derived from drill cuttings (Figure 16c), which shows notable changes at depths of approximately 5, 73, and 130 m. The rough alignment between some of the imaged reflectors and the lithological boundaries supports the effectiveness of the proposed method for field data applications.

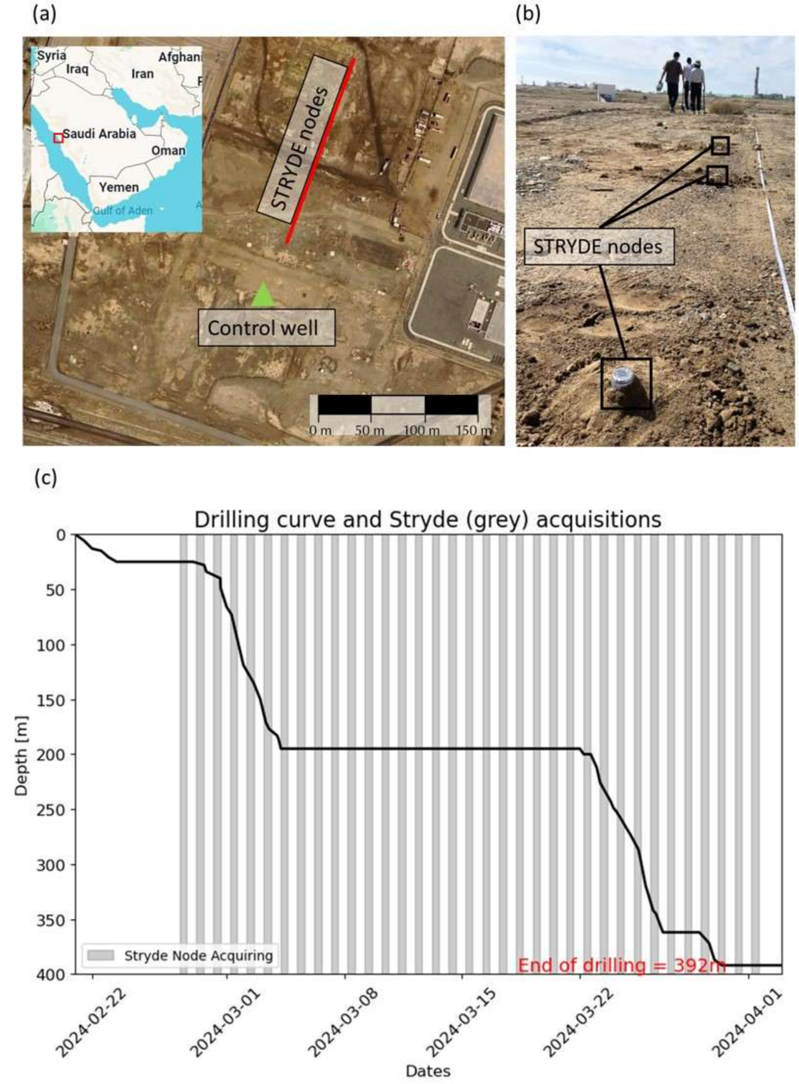

Figure 13. (a) Aerial view of the site alongside the control well (green triangle) and autonomous STRYDE nodes (red solid line). (b) Close-up on the nodes with the wellhead on the upper-right corner of the picture. (c) Drilling depth profile and seismic acquisition time windows.

5 Conclusions

We presented a practical and efficient approach for applying MDD to SWD data, enabling the retrieval of virtual reflection responses that are free from surface-related multiples and source signature effects. Two key innovations of the proposed workflow are i) the use of a PSO-based method to extract the direct arrival components from the recorded continuous wavefield, and ii) the implementation of a segment-based correlation strategy to prepare the input datasets for MDD and ultimately reduce the computational cost of the method whilst maintaining accuracy. The proposed method is first validated through synthetic examples using both acoustic and elastic modeling, demonstrating its ability to suppress artifacts and produce accurate reflection responses and subsurface images, even in the presence of complex and unknown source signatures. Finally, the success-

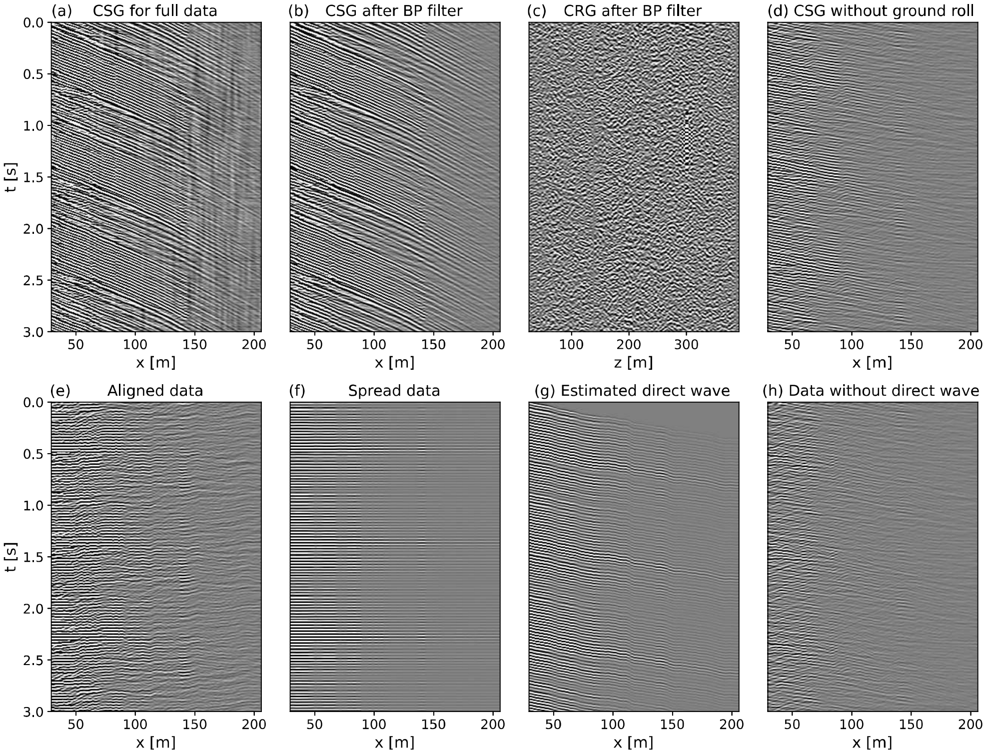

Figure 14. (a) CSG of the full data, (b) CSG after using BP filter, (c) CRG after using BP filter, (d) CSG after without ground roll, (e) aligned wavefield using the optimized time shift, (f) spread wavefield, (g) estimated direct arrival wavefield, (h) wavefield without the direct arrival

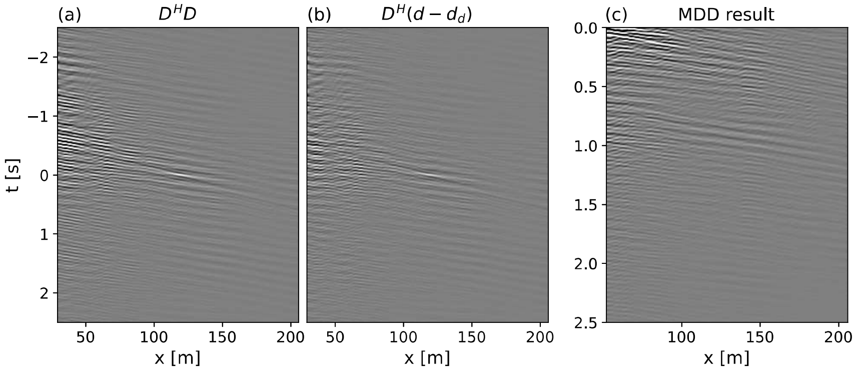

Figure 15. (a) Auto-correlation of the wavefield without ground roll, (b) cross-correlation between the wavefield without ground roll and the wavefield with both the ground roll and direct arrival removed, (c) reconstructed reflection response using MDD.

ful application to a field data set further confirms the robustness, effectiveness, and practicality of this method in field data scenarios. Overall, the proposed method provides a practical and reliable solution for SWD imaging, establishing foundations for future applications in both exploration and real-time subsurface monitoring.

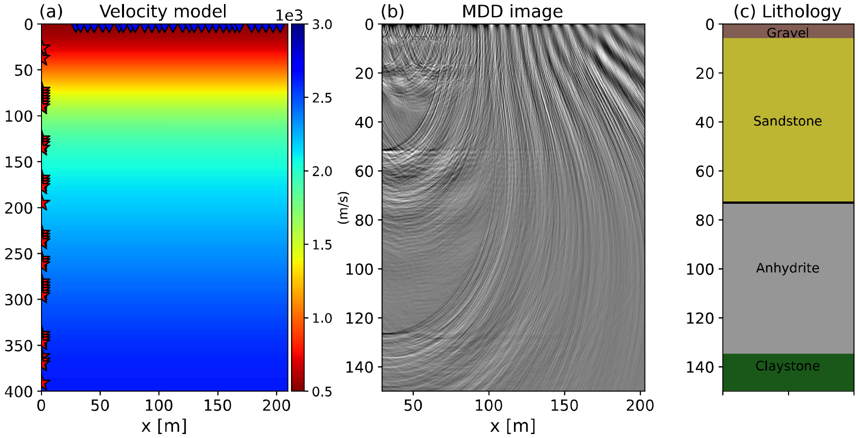

Figure 16. (a) Velocity model used for migration, (b) MDD imaging result, and (c) lithological changes from the drilling report.

Open Research Section

The code supporting the findings of this study will be made available after the paper is published. The model used in the synthetic example is adapted from the open-source SEAM Arid model (Oristaglio, 2015). The field dataset acquired on the KAUST campus will also been made publicly available in accordance with institutional data sharing policies after the paper is published.

Inclusion in Global Research Statement

This research is conducted as part of an academic collaboration based at King Abdullah University of Science and Technology (KAUST), Saudi Arabia. The field dataset used in this study was acquired during a drilling campaign on the KAUST campus, with all necessary permissions and access granted through institutional coordination. No external permits were required for data collection. All contributors who meet the authorship criteria set by AGU Publications are listed as co-authors.

This research aligns with the principles of transparency, fairness, and equitable collaboration as outlined in The TRUST Code. The proposed method aims to support both local and international geophysical communities by promoting accessible, cost-effective and accurate approaches to SWD data processing.

Acknowledgments

This publication is based upon work supported by King Abdullah University of Science and Technology (KAUST) under Award No. RFS-OFP2023-5606. We are grateful to the members of the Deep Imaging Group (DIG) for their support in the data acquisition campaign. We also thank DIG and Seismic Wave Analysis Group (SWAG) for the insightful discussions. AI-based tools (ChatGPT) were used solely for grammar and consistency checking during manuscript preparation, including improving clarity, coherence, and conciseness in the writing process. No AI-generated content was included in the final manuscript.

References

Asgharzadeh, M., Grant, A., Bona, A., & Urosevic, M. (2019). Drill bit noise imaging without pilot trace, a near-surface interferometry example. *Solid Earth*, *10*(4), 1015–1023. Retrieved from `https://se.copernicus.org/articles/10/1015/2019/` doi: 10.5194/se-10-1015-2019

Bakulin, A., Aldawood, A., Silvestrov, I., Hemyari, E., & Poletto, F. (2020). Seismic-while-drilling applications from the first drillcam trial with wireless geophones and instrumented top drive. *The Leading Edge*, *39*(6), 422–429.

Boiero, D., Mahat, S., Bagaini, C., & Ortin, M. (2023). True-amplitude multiple prediction in sparse ocean-bottom acquisitions using a multidimensional deconvolution approach. *84th EAGE Annual Conference and Exhibition*, *2023*(1), 1-5. Retrieved from `https://www.earthdoc.org/content/papers/10.3997/2214-4609.202310695` doi: https://doi.org/10.3997/2214-4609.202310695

Campillo, M., & Paul, A. (2003). Long-range correlations in the diffuse seismic coda. *Science*, *299*(5606), 547-549. doi: 10.1126/science.1078551

Claerbout, J. F. (1968, April). Synthesis of a Layered Medium from its Acoustic Transmission Response. *Geophysics*, *33*(2), 264. doi: 10.1190/1.1439927

de Ridder, S. A. L., & Biondi, B. L. (2013). Daily reservoir-scale subsurface monitoring using ambient seismic noise. *Geophysical Research Letters*, *40*(12), 2969-2974. doi: https://doi.org/10.1002/grl.50594

Galetti, E., Curtis, A., Baptie, B., Jenkins, D., & Nicolson, H. (2017). Transdimensional love-wave tomography of the british isles and shear-velocity structure of the east irish sea basin from ambient-noise interferometry. *Geophysical Journal International*, *208*(1), 36–58.

Goertz, A., Atkinson, B., Thiem, T., & Bergfjord, E. V. (2020). Reservoir imaging-while-drilling with prm arrays. *First Break*, *38*(11), 77–83. Retrieved from `https://doi.org/10.3997/1365-2397.fb2020083` doi: 10.3997/1365-2397.fb2020083

Guy, M. (1961). *Nouvelle methode de controle geologique de forage* (Brevet d'Invention No. 1.584.951). Ministere du Developpement Industriel et Scientifique, Republique Francaise.

Haacke, R., & Poole, G. (2023). Source-side multi-dimensional deconvolution using a downgoing annihilation filter approach. *84th EAGE Annual Conference and Exhibition*, *2023*(1), 1-5. doi: 10.3997/2214-4609.2023628014

Hardage, B. A. (2000). *Vertical seismic profiling: Principles.* Elsevier.

Jardine, S., Lesage, M., & McCann, D. (1990). Estimating tooth wear from roller cone bit vibration. In *Iadc/spe drilling conference.* (IADC/SPE Paper No. 19966)

Katz, L. (1984). *Method and system for seismic continuous bit positioning* (Patent Nos. US 4,460,059). U.S. Patent Office.

Kennedy, J., & Eberhart, R. (1995). Particle swarm optimization. In *Proceedings of ieee international conference on neural networks* (Vol. 4, pp. 1942–1948).

Khaled, O. S., Al-Ateeqi, A. M., James, A. R., & Meehan, R. J. (1996). Seismic-while-drilling in kuwait results and applications. *GeoArabia*, *1*(4), 531–550.

Langenkamp, R. D. (1994). *The illustrated petroleum reference dictionary / edited by robert d. langenkamp.* (4th edition ed.). Tulsa, Oklahoma: PennWell.

Miller, D., Haldorsen, J., & Kostov, C. (1990). *Methods for deconvolution of unknown source signatures from unknown waveform data* (Patent Nos. US 4,922,362). U.S. Patent Office.

Miranda, F., Aleotti, L., Abramo, F., Poletto, F., Craglietto, A., Persoglia, S., & Rocca, F. (1996). Impact of the seismic while drilling technique on exploration wells. *First Break*, *14*(2).

Mordret, A., Rivet, D., Landès, M., & Shapiro, N. M. (2015). Three-dimensional shear velocity anisotropic model of piton de la fournaise volcano (la réunion island) from ambient seismic noise. *Journal of Geophysical Research: Solid Earth*, *120*(1), 406-427. doi: https://doi.org/10.1002/2014JB011654

Naville, C., Serbutoviez, S., Throo, A., Batini, F., Dini, I., & Cecconi, F. (2000).

Drillbit swd reverse walkaway using downhole reference signal. In *Spe/iadc drilling conference.* (SPE Paper No. 65115)

Naville, C., Serbutoviez, S., Throo, A., Vinck, O., & Cecconi, F. (2004). Seismic while drilling (swd) techniques with downhole measurements, introduced by ifp and its partners in 1990-2000. *Oil & Gas Science and Technology*, *59*, 371–403.

Oristaglio, M. (2015). Seam update. *The Leading Edge*, *34*(4), 466-468. doi: 10.1190/tle34040466.1

Picozzi, M., Parolai, S., Bindi, D., & Strollo, A. (2009). Characterization of shallow geology by high-frequency seismic noise tomography. *Geophysical Journal International*, *176*(1), 164–174.

Poletto, F., Bellezza, C., Corubolo, P., Goertz, A., Bergfjord, E. V., & Lindgård, J. E. (2019). Seismic while drilling using a large-aperture ocean bottom array. In *Seg technical program expanded abstracts* (pp. 5320–5324).

Poletto, F., Corubolo, P., & Comelli, P. (2010). Drill-bit seismic interferometry with and without pilot signals. *Geophysical Prospecting*, *58*, 257–265. doi: 10.1111/j.1365-2478.2009.00832.x

Poletto, F., & Dordolo, G. (2002). A new approach to offshore drill-bit rvsp. *Geophysics*, *67*, 1071–1075.

Poletto, F. B., & Miranda, F. (2022). *Seismic while drilling - fundamentals of drill-bit seismic for exploration, 2nd edition.* Elsevier.

Ravasi, M., Selvan, T., & Luiken, N. (2022). Stochastic multi-dimensional deconvolution. *IEEE Transactions on Geoscience and Remote Sensing*, *60*, 1-14. doi: 10.1109/TGRS.2022.3179626

Rector, I., J. W. (1989). *System for reducing drill string multiples in field signals* (Tech. Rep. Nos. 4,862,423). U.S. Patent Office.

Rocca, F., Persoglia, S., Poletto, F., & Craglietto, A. (1990). *Use of drilling noise to generate a reciprocal vsp* (Tech. Rep.). CEE Contract DGXII/TH-0113-87, Final Report of the Project.

Schuster, G. T. (2009). *Seismic interferometry.* Cambridge: Cambridge University Press.

Schuster, G. T. (2014). Seismic interferometry. In *Encyclopedia of exploration geophysics* (pp. Q1-1–Q1-41). Oklahoma, USA: Society of Exploration Geophysicists.

Seeman, B., & Horowicz, L. (1983). Vertical seismic profiling: Separation of upgoing and downgoing acoustic waves in a stratified medium. *GEOPHYSICS*, *48*(5), 555-568. doi: 10.1190/1.1441486

Silvestrov, I., Hemyari, E., Bakulin, A., Luo, Y., Aldawood, A., Poletto, F., … Golikov, P. (2021, November). Processing of seismic-while-drilling data from the drillcam system acquired with wireless geophones, top-drive, and downhole vibrations sensors. *SPE Middle East Oil and Gas Show and Conference*, D031S017R002. doi: 10.2118/204543-MS

Stuart, J. (1989). *Method for determining drill bit wear: European patent application* (European Patent Application No. EP 0 336 477 A1). European Patent Office.

Vasconcelos, I., & Snieder, R. (2008a). Interferometry by deconvolution: part 1 – theory for acoustic waves and numerical examples. *Geophysics*, *73*(3), S115–S128.

Vasconcelos, I., & Snieder, R. (2008b). Interferometry by deconvolution: part 2 – theory for elastic waves and application to drill-bit seismic imaging. *Geophysics*, *73*(3), S129–S141.

Vidal, C. A., & Wapenaar, K. (2014). Passive seismic interferometry by multidimensional deconvolution-decorrelation. *SEG Technical Program Expanded Abstracts*, 2224-2228. doi: 10.1190/segam2014-1208.1

Wang, N., & Ravasi, M. (2023). Upside down Rayleigh-Marchenko imaging: Towards a practical exact redatuming scheme for ocean bottom acquisitions. *Third In-*

ternational Meeting for Applied Geoscience & Energy Expanded Abstracts, 1411-1415.

Wang, N., & Ravasi, M. (2024). Upside-down Rayleigh-Marchenko: a practical redatuming scheme for seabed seismic acquisitions. *Geophysics*, *89*(6), 1-67. doi: 10.1190/geo2023-0743.1

Wapenaar, K., & Fokkema, J. (2006). Green's function representations for seismic interferometry. *Geophysics*, *71*(4), SI33-SI46. doi: 10.1190/1.2213955

Wapenaar, K., van der Neut, J., Ruigrok, E., Draganov, D., Hunziker, J., Slob, E., … Snieder, R. (2011). Seismic interferometry by crosscorrelation and by multidimensional deconvolution: A systematic comparison. *Geophysical Journal International*, *185*(3), 1335–1364.

Weatherby, B. B. (1936). *Method of making sub-surface determinations* (Tech. Rep. Nos. 2,062,151). U.S. Patent Office.

Zhang, Z. d., Alajami, M., & Alkhalifah, T. (2020, 05). Wave-equation dispersion spectrum inversion for near-surface characterization using fibre-optics acquisition. *Geophysical Journal International*, *222*(2), 907-918. doi: 10.1093/gji/ggaa211

Application of Multi-Dimensional Deconvolution to Enhance Seismic-While-Drilling Data Imaging

N. Wang[1], **M. Ravasi**[1,2], **M. Deheuvels**[1], **T. Alkhalifah**[1]

[1]Earth Science and Engineering Program, Physical Science and Engineering Division, King Abdullah
University of Science and Technology (KAUST),Thuwal, 23955-6900, Kingdom of Saudi Arabia
[2]Shearwater GeoServices, London, United Kingdom

Key Points:

- A workflow is developed to apply multi-dimensional deconvolution (MDD) to seismic-while-drilling data, giving virtual reflection responses.
- A direct arrival removal strategy using particle swarm optimization is devised, improving the accuracy of the input wavefields for MDD.
- A segmented correlation strategy is introduced to reduce the cost of MDD, providing stable input for solving the MDD efficiently.

Corresponding author: Ning Wang, `ning.wang.2@kaust.edu.sa`

Abstract

Seismic-while-drilling (SWD) provides a cost-effective solution to sense the subsurface by utilizing the drill-bit noise as a seismic source. However, extracting useful information from SWD recordings remains challenging due to the erratic and unknown nature of the source signature. Thus, we propose a practical workflow for applying multi-dimensional deconvolution (MDD) to SWD data, producing a reflection response from virtual sources to physical receivers at the Earth's surface that is free of surface-related multiples. A key component of the proposed workflow is the estimation of the direct arrival based on the particle swarm optimization algorithm. This technique refines an initial traveltime curve estimate by maximizing the energy of flattened and stacked raw seismic recordings. Moreover, to maintain the computational cost of MDD to a reasonable level, we adopt a strategy commonly used in seismic interferometry whereby auto- and cross-correlation is applied to time segments of the continuous SWD, and the resulting correlograms are stacked together. MDD is then applied using such waveforms as inputs. The proposed methodology is first validated on a range of synthetic data modeled with an acoustic wave equation, demonstrating the improved quality of the retrieved virtual data and images compared to those obtained from standard correlation-based interferometric redatuming. An additional synthetic test using elastic modeling further confirms the robustness of the proposed workflow. Finally, the proposed method is successfully applied to a field dataset. Both the synthetic and field results demonstrate the effectiveness of this workflow, offering a practical and economically viable solution for processing SWD data.

Plain Language Summary

Seismic-while-drilling (SWD) is a method that uses the noise generated by a drill bit as a seismic energy source to image the subsurface. It is cost-effective, but the unpredictable nature of the noise makes it difficult to extract clear seismic signals for accurate imaging. In this study, we develop a novel approach that applies multi-dimensional deconvolution (MDD) to SWD data. This method transforms the noisy recordings into signals as if they came from conventional sources at the Earth's surface, and it removes surface-related multiples. Our workflow includes a new technique to estimate and remove the direct arrivals using an optimization algorithm and introduces a computationally efficient strategy to handle the large volumes of continuous data. Our method was tested on both synthetic and field data. It produced clearer signals and more accurate subsurface images compared to conventional approaches. The technique also proved to be robust and efficient, even when applied to complex geological models and field data. This study provides improved image quality and reduced computational cost for processing SWD data, making it more accessible for subsurface imaging during drilling operations.

1 Introduction

Seismic-while-drilling (SWD) was first proposed by Weatherby (1936) and has recently emerged as a cost-effective solution for subsurface imaging and monitoring due to the fact it eliminates the need for active seismic sources (F. B. Poletto & Miranda, 2022). Unlike conventional vertical seismic profiles (VSP – Hardage (2000)) that use sources on the Earth's surface and record the propagating wavefield within the borehole, SWD relies on the seismic energy naturally generated by the drill bit during drilling and records seismic wavefields by placing sensors on the Earth's surface. Although SWD data typically exhibit a lower signal-to-noise ratio compared to traditional VSP data (F. B. Poletto & Miranda, 2022), this technique presents several advantages. Since SWD does not require the installation of instruments inside a borehole, it reduces the need for drilling interruptions as required by VSP surveys and therefore lowers operational risk. Additionally, it avoids the downtime and costs associated with suspending drilling operations and removing the drill string, which are necessary steps in VSP surveys (Langenkamp, 1994). This allows SWD to provide near-real-time data without interrupting the drilling process. Moreover, by utilizing the continuous seismic energy generated by the drill bit during drilling, SWD can be considered as a form of reverse VSP or drill-bit VSP, enabling seismic data acquisition without the additional cost of deploying dedicated sources. In general, SWD enables efficient, near-real-time data acquisition while avoiding the operational complexity and added cost of deploying downhole sensors. Due to these benefits, SWD has been applied not only in the oil and gas exploration but also in other contexts, including tunnel construction (F. Poletto & Dordolo, 2002) and geothermal exploration (Naville et al., 2000).

The use of drill-bit vibrations as a seismic source has been explored since the 1960s. For instance, Guy (1961) demonstrated that vibrations generated during drilling could be monitored using surface seismometers. Subsequent studies have investigated various applications of drill-bit signals: some researchers used these vibrations to assess the condition of the drill bit itself (Stuart, 1989; Jardine et al., 1990), while others focused on using the signals for subsurface imaging. Katz (1984), for example, developed a method to estimate the drill bit's position by analyzing coherent signals recorded on the surface. Advancements in processing techniques further expanded the potential of SWD. Rector (1989) proposed to auto-correlate the drill-string pilot signal to suppress multiples generated by the drill string. Rocca et al. (1990) explored the use of drill-bit signals for borehole seismic applications by placing pilot sensors on the rig and within the noisy drilling environment. In a field study, Khaled et al. (1996) demonstrated the feasibility of processing SWD data, noting that while the data can be affected by factors such as rock type and drill bit characteristics, it can still produce reliable signals, as shown in their work on the Raudhatain field.

To improve the signal-to-noise ratio of SWD data, researchers often correlate the surface-recorded wavefields with reference pilot signals generated by the drill bit (F. B. Poletto & Miranda, 2022). This approach is conceptually similar to seismic interferometry (SI), a method used to reconstruct the Green's function through cross-correlation of recorded wavefields (Claerbout, 1968; Wapenaar & Fokkema, 2006), which has been successfully applied in various field studies (Campillo & Paul, 2003; Picozzi et al., 2009; de Ridder & Biondi, 2013; Mordret et al., 2015; Galetti et al., 2017). A key difference between dill-bit SWD processing and traditional SI lies in the handling of the source signal. Drill-bit SWD methods typically rely on pilot signals to perform the correlation, while SI does not require any prior knowledge of the source signature. This allows SI to generate virtual sources and reconstruct redatumed surface records directly from the recorded data (Wapenaar & Fokkema, 2006; Schuster, 2009, 2014). The concept of drill-bit SI without pilot signals has also been explored by Miller et al. (1990); Vasconcelos and Snieder (2008a, 2008b), while implementations using pilot signals are presented in studies such as F. Poletto et al. (2010) and Silvestrov et al. (2021). Some other successful field applications further demonstrate the potential of SWD-based methods in both onshore (Miranda et al., 1996; Naville et al., 2004; Bakulin et al., 2020) and offshore environments (F. Poletto et al., 2019; Goertz et al., 2020). These examples highlight the growing interest in SWD as a valuable tool for acquiring additional subsurface information in field drilling projects.

While cross-correlation or single-channel deconvolution-based SI can reconstruct virtual responses and has been used to image the shallow subsurface directly from SWD data (Asgharzadeh et al., 2019), these methods often fail to adequately address surface-related multiples. Moreover, non-ideal illumination conditions can lead to the generation of additional non-physical artifacts in the resulting images. Multi-dimensional deconvolution (MDD) offers a robust alternative solution that can improve the quality of the retrieved Green's function through the deconvolution of the up- and down-going components of the recorded data at a certain datum of interest (Wapenaar et al., 2011). Recent applications of MDD to ocean-bottom data, both on the receiver and source sides, have demonstrated its ability to suppress overburden effects and produce more accurate virtual seismic responses with minimal artifacts (Ravasi et al., 2022; Boiero et al., 2023; Haacke & Poole, 2023; Wang & Ravasi, 2024).

In this study, we propose a novel workflow for multi-dimensional processing and deconvolution of SWD data. The method effectively relocates the seismic source from the drill bit to virtual positions at the Earth's surface, enabling the retrieval of a virtual reflection response that is free from both surface-related multiples and source signature effects. Two key challenges addressed in the proposed workflow are the identification and removal of the direct arrival component from the recorded wavefield, and the application of MDD to long-duration continuous recordings (which can often last several minutes) for each depth point (i.e., source location). To overcome these issues, we develop a data-driven procedure that leverages a global optimization procedure to estimate and remove the direct arrivals. We also propose to solve the normal equations of the MDD problem as this allows us to segment the continuous recordings into smaller time windows, followed by auto- and cross-correlations (which now represents the inputs of the MDD problem). This segmentation and correlation strategy significantly reduces the size of the input wavefields and renders MDD a computationally feasible procedure for SWD data.

The proposed workflow is first validated using synthetic data generated through acoustic modeling using models of increasing structural complexity. Next, to further assess its robustness in field-like conditions, the method is tested on a dataset generated through elastic modeling. The results are compared with those obtained through conventional cross-correlation based redatuming, demonstrating the improved accuracy and reliability of the proposed approach. Finally, the method is applied to a field dataset, and the resulting images reveal structural information that is consistent with the available lithological interpretation from the well cuttings.

2 Theory

2.1 Multi-Dimensional Deconvolution for SWD data

First, let us consider an ocean bottom acquisition geometry, as illustrated in Figure 1a, where sources ($\mathbf{x}_S$) are located just below the sea surface, while both receivers ($\mathbf{x}_R$) and virtual sources ($\mathbf{x}'_R$) are positioned at the sea floor level Λ_R. In this setup, the down-going ($d^+(\mathbf{x}'_R, \mathbf{x}_S)$) and up-going ($d^-(\mathbf{x}_R, \mathbf{x}_S)$) wavefields, propagating from a source ($\mathbf{x}_S$) to receivers ($\mathbf{x}_R$) and virtual sources ($\mathbf{x}'_R$), are related to the local reflection response $R(\mathbf{x}_R, \mathbf{x}'_R)$ via the following multidimensional convolution integral:

$$d^-(\mathbf{x}_R, \mathbf{x}_S) = \int_{\Lambda_R} R(\mathbf{x}_R, \mathbf{x}'_R) d^+(\mathbf{x}'_R, \mathbf{x}_S) d\mathbf{x}'_R, \tag{1}$$

where superscripts (-) and (+) denote the up-going and down-going components, respectively. Here, the local reflection response R represents the seismic response in a medium that is equivalent to the original medium below the datum Λ_R and homogeneous above (i.e., free from interactions with the overburden). The process of solving for R by inverting equation 1 is usually referred to as MDD (Wapenaar et al., 2011; Ravasi et al., 2022).

Since applying receiver-side MDD requires having access to a dense receiver array, which may not always be available in seabed acquisition settings, source-side MDD has been recently proposed as an alternative approach to estimate the local reflection response between source locations (Λ_S) (Vidal & Wapenaar, 2014; Boiero et al., 2023). In this approach, the role of the sources and receivers in Figure 1a is swapped: mirrored receivers are treated as sources, generating the wavefields shown in Figure 1b (Wang & Ravasi, 2023). Based on this reciprocal ocean bottom acquisition geometry, source-side MDD

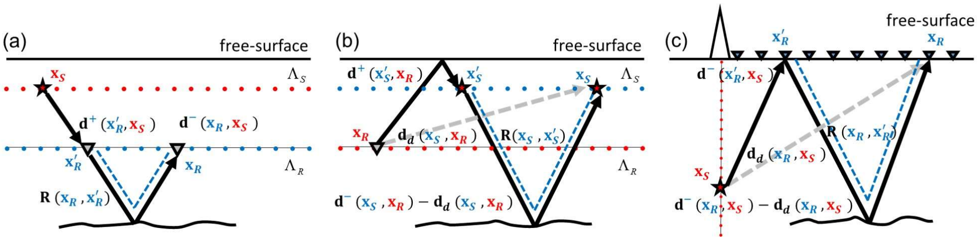

Figure 1. Schematic representation of the wavefields involved in (a) the receiver-side MDD geometry, (b) the source-side MDD geometry, and (c) the SWD geometry. The dashed grey line represents the direct arrival, the dashed blue line represents the reflection response, and the solid black line represents the recorded wavefield.

can be expressed as:

$$\widetilde{d}^-(\mathbf{x}_S, \mathbf{x}_R) = \int_{\Lambda_S} R(\mathbf{x}_S, \mathbf{x}'_S) d^+(\mathbf{x}'_S, \mathbf{x}_R) d\mathbf{x}'_S, \tag{2}$$

where $\mathbf{x}'_S$ represents the virtual receivers, while the superscript $\widetilde{}$ indicates that the wavefield $d^-(\mathbf{x}_S, \mathbf{x}_R)$ is free of the direct arrival component $d_d(\mathbf{x}_S, \mathbf{x}_R)$: $\widetilde{d}^-(\mathbf{x}_S, \mathbf{x}_R) = d^-(\mathbf{x}_S, \mathbf{x}_R) - d_d(\mathbf{x}_S, \mathbf{x}_R)$. Note that the spatial integral is now performed over the source carpet, which is usually regularly and densely sampled.

By moving the virtual receiver array in the reciprocal ocean bottom geometry (blue dots in Figure 1b) to the location of the free surface, the source-side MDD geometry aligns with that of an SWD experiment, as shown in Figure 1c. In this case, the sources located in the well can be interpreted as virtual sources mirrored by the free surface. As a result, only the up-going wavefield on the source side is considered in the MDD formulation. As illustrated in Figure 1c, the up-going wavefield on the source side ($d^-(\mathbf{x}'_R, \mathbf{x}_S)$) is convolved with the local reflection response ($R(\mathbf{x}_R, \mathbf{x}'_R)$) to generate the total up-going wavefield without the direct arrival ($d^-(\mathbf{x}_R, \mathbf{x}_S) - d_d(\mathbf{x}_R, \mathbf{x}_S)$):

$$d^-(\mathbf{x}_R, \mathbf{x}_S) - d_d(\mathbf{x}_R, \mathbf{x}_S) = \int_{\Lambda_R} R(\mathbf{x}_R, \mathbf{x}'_R) d^-(\mathbf{x}'_R, \mathbf{x}_S) d\mathbf{x}_R. \tag{3}$$

By solving equation 3 for R, sources originally located within the well can be effectively relocated to the same position of the surface receivers. The retrieved local reflection response R is moreover free from surface-related multiples and source signature effects.

In practice, equation 3 is discretized over both the time and spatial axes and represented in the following compact matrix-vector notation:

$$\mathbf{d}^- - \mathbf{d}_d = \mathbf{D}^-\mathbf{r}, \tag{4}$$

where $\mathbf{r}$ represents the reflection response to be recovered, and $\mathbf{D}^-$ is a multi-dimensional convolutional operator whose integral kernels contains an ensemble of continuous recordings $d^-(\mathbf{x}'_R, \mathbf{x}_S)$, one for each source location in the wellbore.

2.2 Pre-processing workflow of SWD data

To apply equation 4 to SWD data, the recorded wavefield must first be decomposed into up- and down-going components on the source side, and the direct arrival must be removed from the up-going wavefield. The proposed pre-processing workflow therefore consists of two main steps: i) removing the down-going wavefield from the source side, and ii) removing the direct arrivals from the up-going wavefield. The first step is typically achieved by transforming each common-receiver gather (CRG) into the frequency-wavenumber (f-k) domain and separating wavefield components based on their apparent slowness, which is a standard technique in VSP data processing (Seeman & Horowicz, 1983). However, this step is not straightforward in practice due to the unknown start time of the source wavelet. In this paper, we assume the first step is feasible in the first two synthetic examples presented in the next section, in order to establish a benchmark. In the third test presented in the Synthetic Examples section, we investigate the implications of skipping this step by presenting results without this pre-processing, to evaluate the robustness of the MDD approach under more realistic, field-like conditions. The second step addresses the removal of the direct arrival from the up-going wavefield. Unlike in traditional active-seismic experiments, the SWD source signature is random and usually unknown, unless a sensor is deployed near the drill bit. As a result, conventional direct arrival removal methods are not applicable.

Instead, to accurately identify and remove the direct arrival component from raw SWD data, we employ a global optimization method – specifically, particle swarm optimization (PSO – Kennedy and Eberhart (1995)), to obtain an estimate of the direct traveltime curve $\tau(x_r)$ from the source in the well-bore to the surface receivers, which optimally aligns and stacks the continuous recording along the receiver aperture. The procedure begins by flattening a continuous recording (i.e., a common-shot like gather – CSG) using an initial traveltime estimate, $\tau_0(x_r)$, which can be analytically computed from a constant velocity model or numerically computed from a smoothly varying velocity model. This initial estimate is refined within the PSO framework by applying small, randomized time shifts to each trace and maximizing the squared L_2 norm of the stacked flattened CSG – or equivalently, minimizing its negative squared L_2 norm. This formulation is based on the fact that the direct arrival typically exhibits the highest amplitude in the CSG. The optimization process aims to determine the true direct traveltime curve by ensuring that the CSG flattened using the refined traveltime of the direct arrival presents events associated with the direct component of the wavefield as flat as possible, thereby maximizing the amplitude of the stacked wavefield. To ensure physically reasonable and smooth variations in the estimated traveltime curve, a regularization term is added to constrain the time-shift differences between adjacent traces ($\mathrm{diff}(\tau(x_r))$), limiting abrupt changes and promoting lateral continuity in the final traveltime estimate. The overall optimization problem is therefore formulated through the following objective function:

$$\arg\min_{\tau(x_r)} -\|\sum_{x_r} d(t-\tau(x_r), x_r)\|_2^2 + \alpha \left\|\mathrm{diff}(\tau(x_r))\right\|_2^2 , \tag{5}$$

where α is a regularization parameter.

PSO is a population-based stochastic algorithm designed to solve high-dimensional, non-convex optimization problems. Inspired by the collective behavior of bird flocks searching for food, PSO explores the solution space through a swarm of candidate solutions known as particles. In this study, each particle represents a vector of traveltime shifts applied to the different traces within a CSG. These shifts are iteratively adjusted to minimize the objective function defined in equation 5. During each iteration, the position and velocity of each particle are updated based on a combination of its personal best solution and the global best solution found by the swarm. The particle's velocity determines the step size and direction of movement within the search space, while its position corresponds to a candidate solution. The updated position (traveltime shift) for the i-th particle at iteration $k+1$, is given by:

$$\tau_i^{(k+1)}(x_r) = \tau_i^{(k)}(x_r) + v_i^{(k+1)}(x_r), \tag{6}$$

where i denotes the particle index, and k represents the iteration number. The term $\tau_i^{(k)}(x_r)$ represents the current position of particle i, which in this context represents a set of traveltime shifts applied to the traces in a CSG. The term $v_i^{(k)}(x_r)$ is the corresponding current velocity (or adjustment of position), dictating the direction and magnitude of change in the solution space. The updated position $\tau_i^{(k+1)}(x_r)$ represents the new set of traveltime shifts for the next iteration. In this study, the dimensionality of each particle equals the number of traces in a CSG, as each trace requires an independent shift to be optimized.

The particle velocity controls how quickly particles explores the solution space. A high velocity enhances exploration, allowing particles to search a broader range of candidate solutions, though this may increase the risk of overshooting the optimal solution. In contrast, a low velocity promotes local exploitation, enabling finer adjustments around promising areas but with a higher likelihood of getting trapped in local optima. The velocity update is computed using the following equation:

$$v_i^{(k+1)}(x_r) = \omega v_i^{(k)}(x_r) + \phi_p r_p (p_i^{(k)}(x_r) - \tau_i^{(k)}(x_r)) + \phi_g r_g (g^{(k)}(x_r) - \tau_i^{(k)}(x_r)). \tag{7}$$

This expression consists of three main components. The inertia term, $\omega v_i^{(k)}(x_r)$, represents a weighted contribution of the particle's previous velocity, maintaining momentum. The cognitive term, $\phi_p r_p (p_i^{(k)}(x_r) - \tau_i^{(k)}(x_r))$, attracts the particle toward its own best-known position, encouraging self-guided refinement. The social term, $\phi_g r_g (g^{(k)}(x_r) - \tau_i^{(k)}(x_r))$, encourages movement toward the globally optimal solution found by the swarm, promoting collective intelligence. Here, the parameter ω is the inertia weight, which balances exploration and exploitation: a larger ω enhances the global search ability, while a smaller ω promotes faster convergence. The variables r_p and r_g are uniformly distributed random numbers between 0 and 1, introducing stochastic variability into the search process. The coefficients ϕ_p and ϕ_g determine the influence of personal versus global best positions, respectively. Finally, the variable $p_i^{(k)}(x_r)$ denotes the best-known position of particle i, while $g^{(k)}(x_r)$ represents the best position found by the entire swarm up to iteration k.

Once the optimal time shifts are determined, each CSG is flattened using the final traveltime curve. This process flattens the continuous train of direct arrivals, which typically corresponds with the events of strongest amplitude, while other seismic events appear curved. As a result, when the flattened CSG is stacked into a single trace, the direct arrival constructively reinforces due to its consistent polarity, whereas other events, containing both positive and negative amplitudes, tend to cancel out. The resulting stacked trace, which predominantly represents the direct arrival, is then redistributed across all receiver positions and each trace is shifted back to its original travel time, yielding an estimate of the direct arrival. Finally, the estimated direct arrival is adaptively subtracted from the up-going wavefield, resulting in the up-going component without the direct arrivals.

2.3 MDD implementation

The local reflection response in equation 3 ideally requires the full up-going wavefield and its counterpart with the direct arrival removed, denoted as $\mathbf{d}^-$ and $\mathbf{d}^- - \mathbf{d}_d$, respectively. However, in practice, due to the slowly moving drill-bit, one can safely assume that the SWD recording for each 'stationary' source location in the wellbore can last up to several minutes; using several or such recordings to form the MDD equations can therefore results in a prohibitively high memory consumption.

To circumvent this, we propose here to solve the normal equations of the MDD problem:

$$\mathbf{D}^H(\mathbf{d}^- - \mathbf{d}_d) = (\mathbf{D}^H\mathbf{D}^-)\mathbf{r}. \tag{8}$$

However, under the assumption that the auto- and cross-correlation of $\mathbf{d}^-$ and $\mathbf{d}^- - \mathbf{d}_d$ have a decorrelation length in the order of some seconds, much shorter time recordings can be effectively used as input to the MDD process. Moreover, as commonly done in

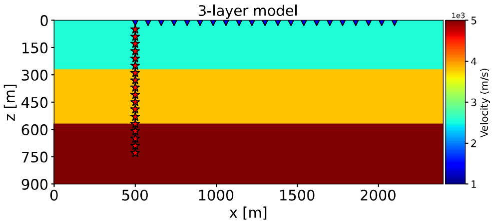

Figure 2. Three-layer velocity model. Red stars represent sources positions within a well, and blue triangles represent surface receivers locations.

standard seismic interferometric process (Zhang et al., 2020), the continuous processed wavefields ($\mathbf{d}^-$ and $\mathbf{d}^- - \mathbf{d}_d$) are divided into time segments with a duration of only a few seconds ($\mathbf{d}_i^-$ and $\mathbf{d}_i^- - \mathbf{d}_{d,i}$), where i denotes the segment index. Auto- and cross-correlation are then performed for each segment individually and the resulting correlated wavefields are stacked together. In other words, this corresponds to applying the adjoint of the modeling operator with the up-going wavefield ($\mathbf{D}_i^H$) to both sides of equation 3 independently for each segment and stacking the results from all segments:

$$\sum_i \mathbf{D}_i^H (\mathbf{d}_i^- - \mathbf{d}_{d,i}) = \sum_i (\mathbf{D}_i^H \mathbf{D}_i^-)\mathbf{r}. \tag{9}$$

This approach produces an approximate representation of the wavefields $\mathbf{D}^H(\mathbf{d}^- - \mathbf{d}_d)$ and $\mathbf{D}^H\mathbf{D}^-$. To our knowledge, this strategy, although very popular in the field of seismic interferometry, it has not previously been applied within the context of MDD. Incorporating this step significantly improves the clarity of the input data for the normal MDD equation (equation 9) compared to the original SWD MDD equation 4, and ultimately facilitates a more stable and easier MDD process. Additionally, the segmentation approach enables MDD to be performed on a much smaller dataset, significantly reducing both memory and computational costs.

3 Synthetic examples

To demonstrate the effectiveness of the proposed method, we first apply it to a set of synthetic data sets generated using acoustic modeling. This provides a controlled environment to validate each step of the workflow. We then apply the method to a data set modeled with elastic wave propagation to mimic a more realistic setting closer to that expected in field conditions.

3.1 Three-layer model

To clearly illustrate the pre-processing workflow, we begin with a simple three-layer acoustic model (Figure 2). The acquisition setup includes 401 surface receivers spaced every 4 m between 500 and 2100 m, represented by blue triangles in Figure 2, and 351 sources placed along a vertical borehole from 50 to 750 m at 2 m intervals, represented by red stars. To simulate a realistic SWD data set, seismic data are first modeled using an impulsive source with free-surface effects included. The resulting data are then convolved with a source signature composed of 3 minutes of white Gaussian noise, mimicking the continuous nature of drill-bit energy. A 1.5 s close-up of a representative CSG from a source depth of 150 m is shown in Figure 3a.

To apply the proposed method, we first arrange the data set into the CRG for processing as shown in Figure 3b. Wavefield separation is then performed in the f-k domain

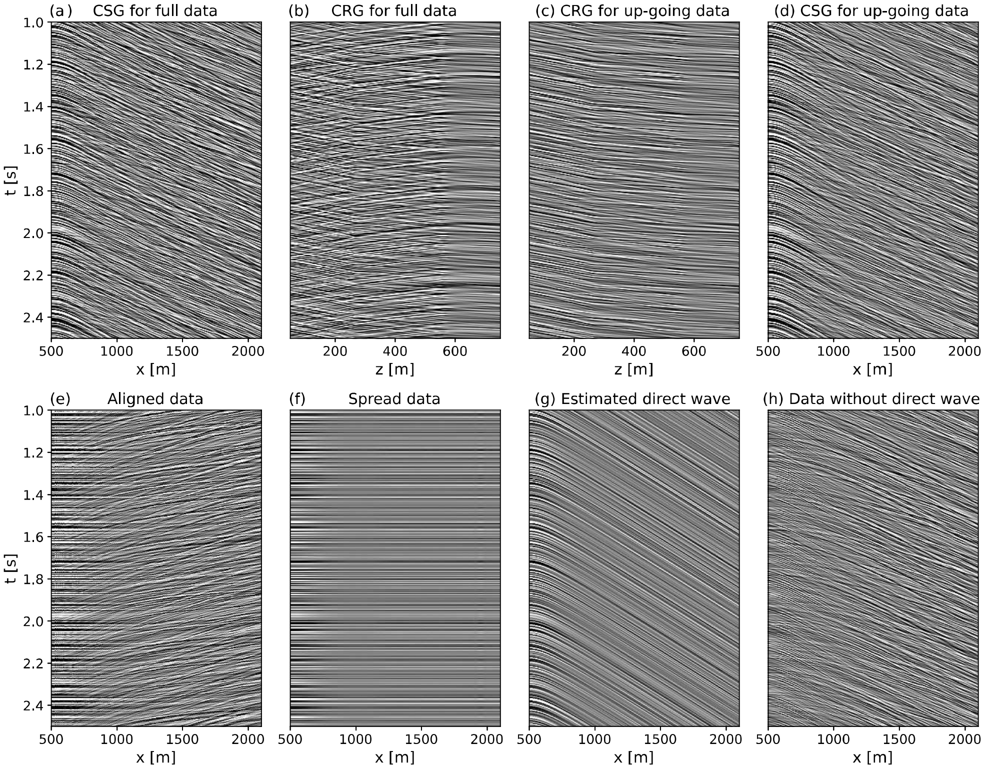

Figure 3. (a) CSG of the full data, (b) CRG of the full data, (c) CRG of the the up-going wavefield, (d) CSG of the the up-going wavefield, (e) aligned wavefield using the optimized time shift, (f) stacked direct arrival trace spread across the entire receiver array, (g) estimated direct arrival wavefield, (h) up-going wavefield after direct arrival removal via adaptive subtraction.

based on slowness, removing the down-going component. The resulting up-going component is shown in CRG and CSG formats in Figures 3c and 3d, respectively. Next, PSO-based alignment method is applied to each up-going CSG to flatten the direct arrival (Figure 3e). The aligned wavefield is then stacked and re-distributed across all traces to suppress events other than direct arrival, producing the wavefield shown in Figure 3f. Shifting this re-distributed trace back to its original traveltime positions yields the estimated direct arrival (Figure 3g). Finally, the estimated direct arrival is removed from the up-going wavefield using adaptive subtraction, yielding an approximation of the coda of the up-going wavefield (i.e., up-going wavefield deprived of the contribution of the direct arrivals) as shown in Figure 3h. To manage the large volume of continuous data, the 3-minute recording is divided into 4-second segments. For each segment, cross-correlation is performed between the up-going wavefield and the up-going wavefield with the direct arrival removed, while auto-correlation is applied to the original up-going wavefield. The resulting correlegrams from all of the different segments are then summed together to produce the input wavefields for normal equations of the MDD process, as shown in Figures 4a and 4b.

Subsequently, the local reflection response is obtained through MDD (Figure 4d); note how this free of surface-relate multiples and source signature effects. For comparison, the wavefield obtained using conventional cross-correlation is also presented in Figure 4e. This result is also free from source signature effects, however, several free-surface

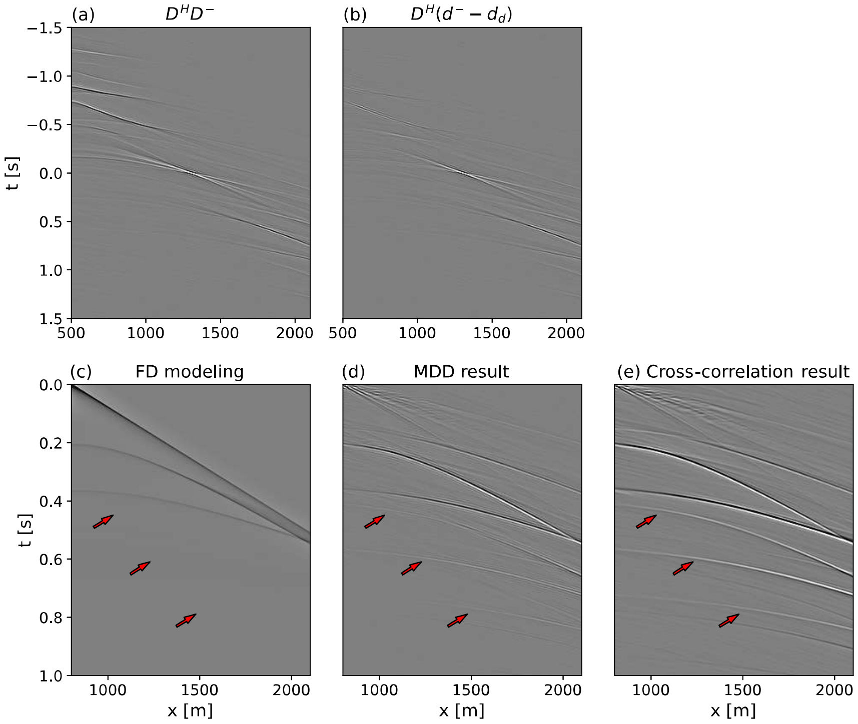

Figure 4. (a) Auto-correlation of the up-going wavefield, (b) cross-correlation between the up-going wavefield and the up-going wavefield with the direct arrival removed. Reconstructed wavefields using (c) FD modeling, (d) MDD, and (e) cross-correlation.

multiples are still present (red arrows in Figure 4e). Additionally, a reference solution is computed using finite-difference (FD) modeling without free-surface effects, employing an impulsive source and positioning both sources and receivers at the Earth's surface (a shot gather from it is shown in Figure 4c). It is important to note that both the MDD and cross-correlation results represent single-sided wavefields, propagating from the well towards increasing positive offsets. This asymmetry arises from the geometry of the SWD acquisition (Figure 1c), as sources are located in the well and energy propagates away from it. As a result, the local reflection response lacks contributions from virtual sources to receivers that lie on either side of the wellbore. Therefore, here we only present the resulting wavefield arranged as CSGs with a virtual source positioned at x = 800 m and receivers placed on the far side of the well, covering the range from x = 800 to 2100 m. Compared to the reference result, the MDD output successfully reconstructs both primary reflection responses, while the cross-correlation result contains noticeable artifacts, as indicated by the red arrows in Figures 4c–4e.

To further assess imaging quality, the wavefields obtained from all three methods are imaged using pre-stack Kirchhoff depth migration. As shown in Figure 5, image produced from MDD (Figure 5b) closely matches the reference image derived from FD modeling (Figure 5a). It successfully recovers both reflectors and effectively suppresses multiple-related artifacts, which remain visible in the image generated from the cross-correlation result (Figure 5c). These results validate the effectiveness of the proposed method in accurately recovering the reflection response while handling both the unknown source signature and surface-related multiples.

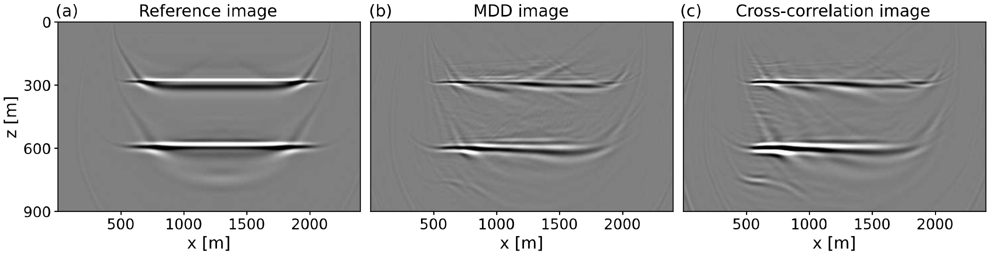

Figure 5. Imaging results obtained from data modeled using (a) FD modeling, (b) MDD, and (c) cross-correlation.

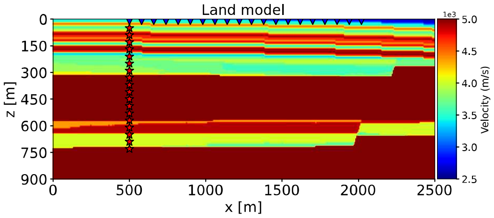

Figure 6. Land velocity model. Red stars represent sources positions within a well, and blue triangles represent surface receivers locations.

3.2 Land model

Next, we apply the proposed method to a more geologically complex land model (Figure 6), adapted from the SEAM Arid model (Oristaglio, 2015). This model features numerous faults and high-contrast layers, providing a more realistic test for the proposed workflow. A vertical well is placed at x = 500 m, where 351 sources are placed along the borehole at 2 m intervals from depths of 50 to 750 m (shown as red stars in Figure 6). On the surface, 401 receivers are deployed with 4 m spacing, spanning from 500 to 2100 m (represented by the blue triangles). Following the same procedure described in the previous example, seismic data are first simulated using an impulsive source with free-surface effects included and then convolved with a source signature consisting of 3-minutes white Gaussian noise.

The pre-processing workflow for this example is also the same as the one described for the three-layer model. We begin by removing the source-side down-going component of the wavefield; this is followed by the PSO-based alignment process to estimate and subtract the direct arrival. Next, the processed three-minute recording is divided into four-second segments. For each segment, correlations are performed and then summed to generate the input wavefields required to solve the normal equations of the MDD problem, as shown in Figure 7a and 7b. Due to the complex subsurface structure, the wavefields are clearly more intricate than those from the simple three-layer model. The local reflection response obtained through MDD using the processed data and the cross-correlation result are shown in Figure 7d and 7e, respectively. Compared to the reference reflection response without free surface effect produced by FD modeling with co-located sources and receivers on the surface (Figure 7c), both MDD and cross-correlation results contain artifacts, with the cross-correlation result showing more pronounced ringing as indicated by the red arrow. Subsequently, Kirchhoff migration is applied to the three different wavefields. Both the MDD (Figure 8b) and the cross-correlation (Figure 8c) images capture the main subsurface structures and are in good agreement with the

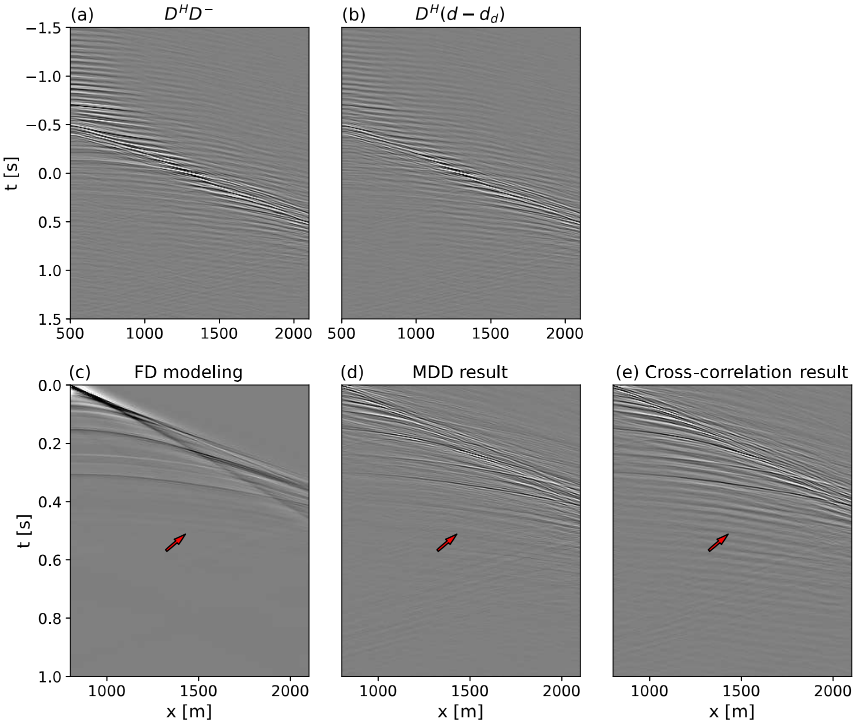

Figure 7. (a) Auto-correlation of the up-going wavefield, (b) cross-correlation between the up-going wavefield and the up-going wavefield with the direct arrival removed. Reconstructed wavefields using (c) FD modeling, (d) MDD, and (e) cross-correlation.

reference image from FD modeling (Figure 8a). However, the cross-correlation image displays more noticeable artifacts, again highlighted by red arrows. Moreover, some of the far-offset structures within the yellow squares (Figure 8), exhibit reduced illumination compared to the near-offset region. This limitation arises from insufficient receiver coverage. Similarly, deeper subsurface features, marked by the blue squares, are poorly resolved due to limited contribution from deeper sources, which are essential for illuminating these areas effectively. It is important to note that these limitations are not a shortcoming of the proposed method, rather inherent to the SWD acquisition geometry. Despite these challenges, the results demonstrate the ability of the proposed method to suppress artifacts and improve image quality in complex geological environments. Compared to the conventional cross-correlation approach, which produces noisier results with more visible artifacts, the MDD-based method offers clearer, more accurate images.

3.3 Three-layer model by elastic modeling

In real-life scenarios, the wavefield generated by the drilling bit is more complex due to the elastic nature of the subsurface. To evaluate the practicality of the proposed method under more realistic conditions, we apply it to synthetic data generated using elastic wavefield modeling.

Another key challenge we face in real data is the application of wavefield separation on the source side. In the previous tests, each source shared the same 3-minute random noise signature, allowing for coherent wavefield construction in the CRG domain. However, in practice, the drill-bit-generated noise varies for each source, making the recorded

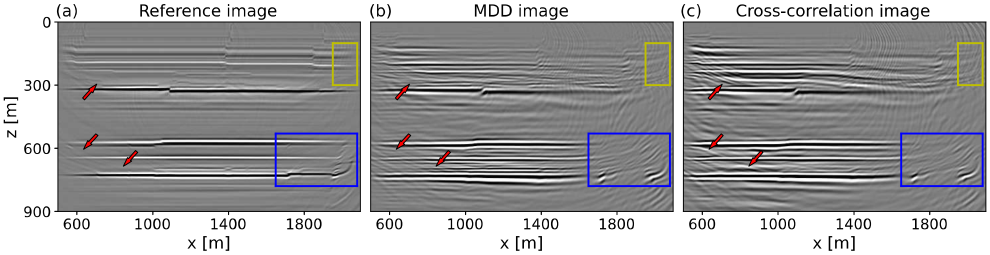

Figure 8. Imaging results obtained by (a) FD modeling, (b) MDD and (c) cross-correlation.

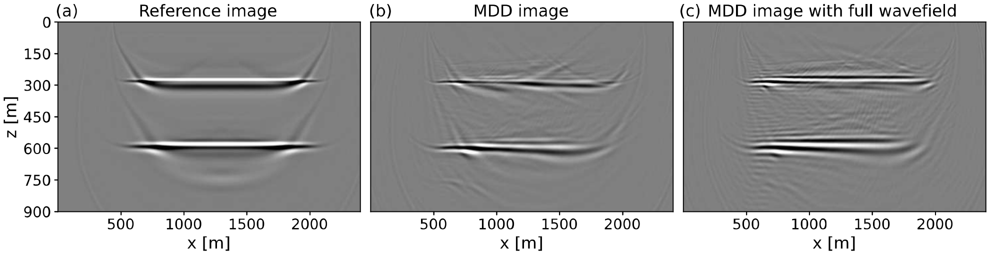

Figure 9. Imaging results obtained from data modeled using (a) FD modeling, (b) MDD with only up-going component on the source side, and (c) MDD with full wavefield.

wavefield incoherent from trace to trace. As a result, wavefield separation using slowness-based methods becomes infeasible for field data. While ideal in theory, wavefield separation is not practical for field scenarios.

Fortunately, a previous example shows that the down-going component of the wavefield is typically much weaker than the up-going wavefield, making the full wavefield (Figure 3a) and up-going wavefield (Figure 3d) looks pretty much similar. Thus, omitting this step in the processing workflow might have a negligible impact on the final result, as demonstrated in Figure 9c, which accurately depicts the two main layers seen in the reference image (Figure 9a) accurately and closely matches the MDD imaging result obtained using only the up-going component on the source side (Figure 9b).

Next, we present a test using the same three-layer model and acquisition geometry shown in Figure 2, but simulated using elastic modeling. Here, each source is assigned a unique 3-minute white Gaussian noise signal to reflect the variability observed in real drill-bit operations, while free-surface effects are also included in the modeling. A representative CSG is shown in Figure 10a. Compared to its acoustic counterpart (Figure 3a), the elastic data set contains an additional prominent component: the ground roll, which dominates the wavefield with strong energy. Figure 10b presents a CRG constructed using different source signatures. In contrast to the CRG with identical source signatures in Figure 3b, the wavefield appears incoherent and noisy, preventing successful wavefield separation. To suppress the ground roll, every CSG is transformed into the f-k domain, where components are separated based on their apparent slopes. The resulting wavefield without ground roll arranged as CSG is shown in Figure 10c. This wavefield more closely resembles the acoustic wavefield in Figure 3d, though it contains slightly more converted wave energy and some residual ground roll, as indicated by the red arrows in Figure 10c. As expected, the corresponding CRG (Figure 10d) remains noisy due to the incoherent source signatures. Subsequently, each CSG is flattened using the PSO-based alignment method, as shown in Figure 10e. The aligned wavefield is then stacked and spread across

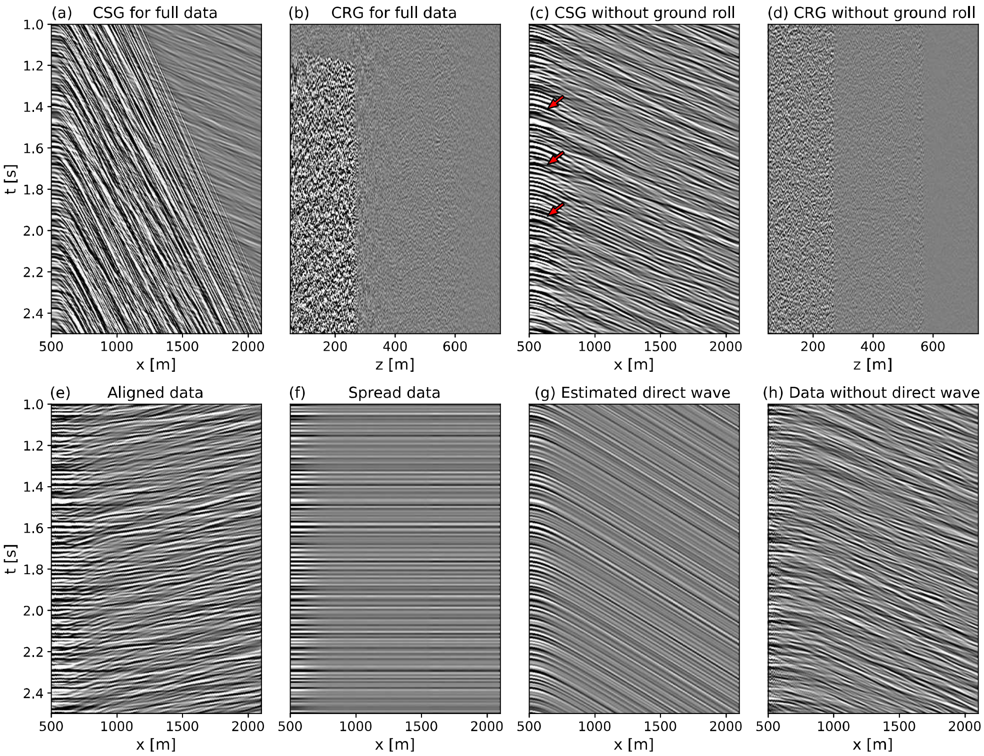

Figure 10. (a) CSG of the full data, (b) CRG of the full data, (c) CSG without ground roll, (d) CSG without ground roll, (e) aligned wavefield using the optimized time shift, (f) spread wavefield, (g) estimated direct arrival wavefield, (h) wavefield without the direct arrival

all traces (Figure 10f), followed by shifting the result back to reconstruct the estimated direct arrival (Figure 10g). The total wavefield without the direct arrival is then obtained by adaptive subtraction as shown in Figure 10h. Compared to the acoustic case (Figure 3h), the elastic result contains more residual artifacts, primarily due to the influence of ground roll. In this example, a simple filtering approach is used to suppress the ground roll, which yields an acceptable result but could be further improved using more advanced suppression techniques. Next, the segmentation method is applied to the 3-minute recordings, which is followed by correlation and summation to produce the final input wavefield for normal MDD, as shown in Figures 11a and 11b. As expected, these inputs contain more noise than those obtained from acoustic modeling.

The local reflection response is then retrieved using MDD applied to the processed elastic data, as shown in Figure 11d, and cross-correlation result is shown in Figure 11e. Both of the MDD and cross-correlation results successfully recover two key reflections while showing additional artifacts caused by the imperfect removal of the ground roll as indicated by yellow arrows, which is non-present for the acoustic MDD result as shown in Figures 11c. Additionally, the cross-correlation result contains free-surface related artifacts than the MDD result as indicated by the red arrows in Figure 11e.

Finally, the reconstructed wavefields are used to carry out Kirchhoff migration, producing images shown in Figure 12b and Figure 12c. For reference, the migration result from the acoustic MDD case is also included (Figure 12a). The image produced from the elastic MDD wavefield matches quite well that of the acoustic reference MDD wavefield,

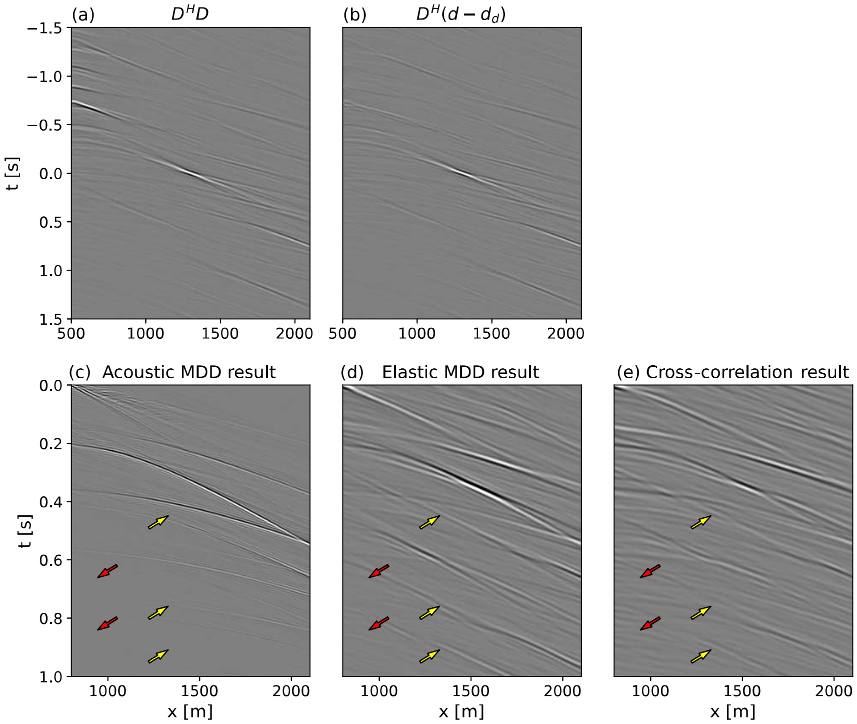

Figure 11. (a) Auto-correlation of the wavefield without ground roll, (b) cross-correlation between the wavefield without ground roll and the wavefield with both the ground roll and direct arrival removed. Reconstructed wavefields using (c) MDD by acoustic modeling, (d) MDD, and (e) cross-correlation.

describing the two layers correctly, however, with some artifacts remaining as marked by the yellow arrow in Figure 12b. As observed in previous examples, the cross-correlation result again exhibits more artifacts than the MDD counterpart, particularly at far offsets and within the second layer, which is poorly imaged as indicated by the red arrow in Figure 12c.

This example highlights two key distinctions relative to the acoustic case: first, ground roll is present due to elastic wave propagation and must be suppressed; second, wavefield separation on the source side was omitted to mimic the conditions of a realistic SWD experiment, where the source signature varies across locations, and yet we obtained good resultds. If more advanced techniques were employed to attenuate ground roll or even converted wave energy, the final results could be further improved. Overall, these results demonstrate the robustness of the proposed method when applied to realistic data sets, even in the presence of down-going wavefield components on the source side. This supports its applicability to field data.

4 Field example

Finally, the proposed method is applied to a field data set acquired at a site located at King Abdullah University of Science and Technology in Saudi Arabia. As shown in Figure 13a, a pilot well (marked by the green triangle) was drilled to a depth of 392 m for monitoring purposes. A total of 89 STRYDE nodes were deployed along a 176-meter-

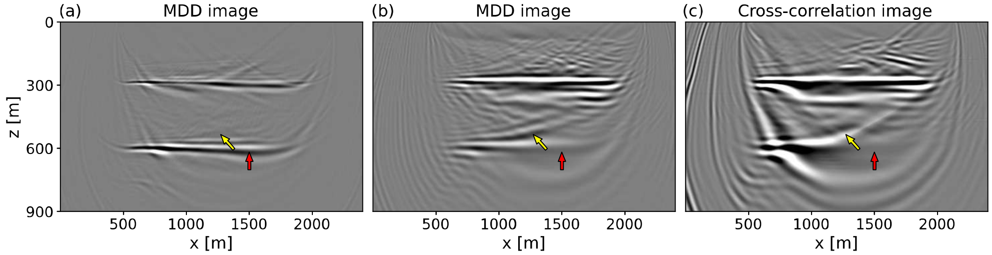

Figure 12. Imaging results obtained by (a) MDD by acoustic modeling, (b) MDD and (c) cross-correlation.

long 2D surface line (shown as the red solid line in Figure 13a), with approximately 2-meter spacing between receivers. These nodes (shown as in Figure 13b) recorded the vertical component of the particle acceleration vector continuously over the course of the drilling operation. According to the drilling report and the STRYDE acquisition schedule shown in Figure 13c, 115 effective SWD source locations were selected for processing, each comprising 8 minutes of continuous recording.

The field data processing flow begins with the application of a band-pass (BP) filter to the original SWD recordings (Figure 14a), removing frequencies below 5 Hz and above 40 Hz. This step attenuates low-frequency ambient noise and high-frequency interference, resulting in a cleaner wavefield, as shown in Figure 14b. When this filtered data is arranged in a CRG configuration, it remains incoherent and noisy (Figure 14c), confirming the earlier observation that wavefield separation on the source side is not feasible for SWD raw data due to inconsistent source signatures. To further suppress coherent surface noise generated by the drilling rig, the filtered data are transformed into the f-k domain and masked, leading to a cleaner wavefield as shown in Figure 14d. Following this step, each CSG is aligned using the PSO-based method (Figure 14e). The aligned wavefield is stacked and redistributed across all traces (Figure 14f), followed by time-shifting to reconstruct the estimated direct arrival (Figure 14g). The estimated direct arrival is then adaptively subtracted, yielding the wavefield without the direct component, as shown in Figure 14h. As in the synthetic examples, the 8-minute processed data sets are divided into 4-second segments. Each segment is correlated and then summed to produce the input wavefields for solving the normal MDD equation, as shown in as shown in Figures 15a and 15b. The final reflection response retrieved through MDD is presented in Figure 15c.

Since the nodes acquired data for only 10 hours a day during the drilling campaign (aside from a nearly month-long pause in the middle of the campaign), the source distribution is irregular, as indicated by the red stars in Figure 16a. The final imaging result is obtained by migrating the reflection response retrieved through MDD using Kirchhoff depth migration. The initial velocity model used for migration (Figure 16a) was derived from a previously acquired active seismic survey. The resulting image, presented in Figure 16b, reveals the presence of four key reflectors at depths of approximately 5, 17, 53, and 126 m. To validate the imaging results, a comparison is made with the lithological profile derived from drill cuttings (Figure 16c), which shows notable changes at depths of approximately 5, 73, and 130 m. The rough alignment between some of the imaged reflectors and the lithological boundaries supports the effectiveness of the proposed method for field data applications.

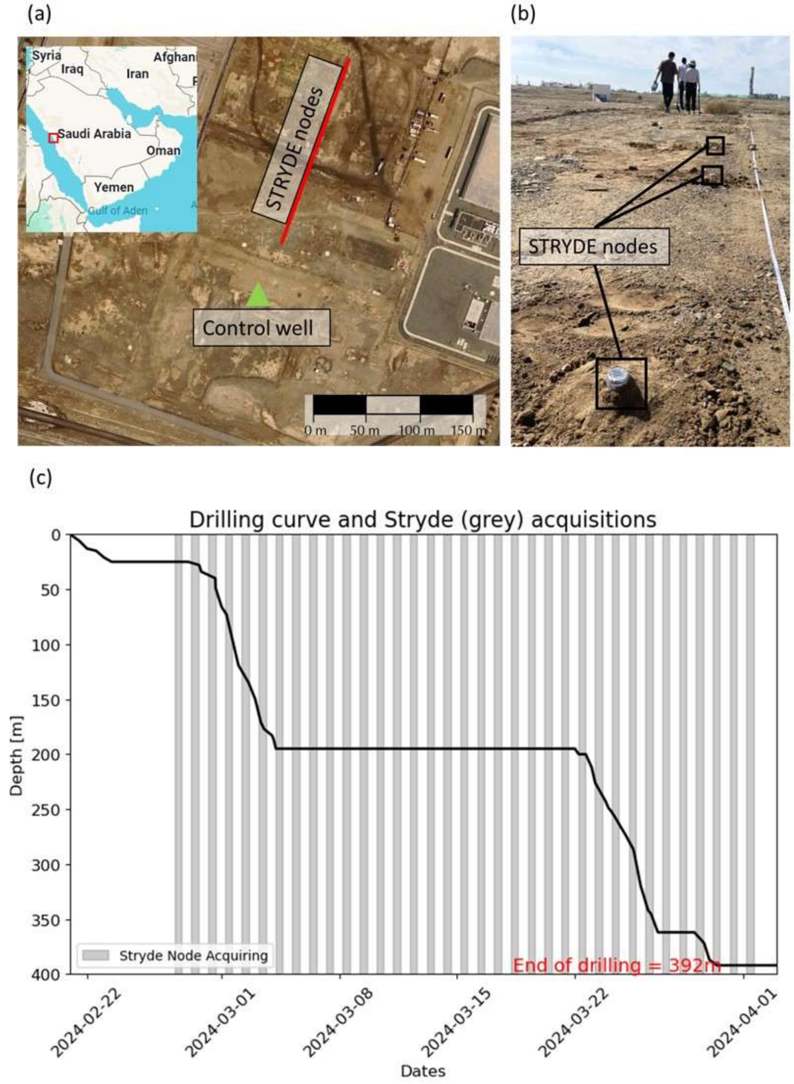

Figure 13. (a) Aerial view of the site alongside the control well (green triangle) and autonomous STRYDE nodes (red solid line). (b) Close-up on the nodes with the wellhead on the upper-right corner of the picture. (c) Drilling depth profile and seismic acquisition time windows.

5 Conclusions

We presented a practical and efficient approach for applying MDD to SWD data, enabling the retrieval of virtual reflection responses that are free from surface-related multiples and source signature effects. Two key innovations of the proposed workflow are i) the use of a PSO-based method to extract the direct arrival components from the recorded continuous wavefield, and ii) the implementation of a segment-based correlation strategy to prepare the input datasets for MDD and ultimately reduce the computational cost of the method whilst maintaining accuracy. The proposed method is first validated through synthetic examples using both acoustic and elastic modeling, demonstrating its ability to suppress artifacts and produce accurate reflection responses and subsurface images, even in the presence of complex and unknown source signatures. Finally, the success-

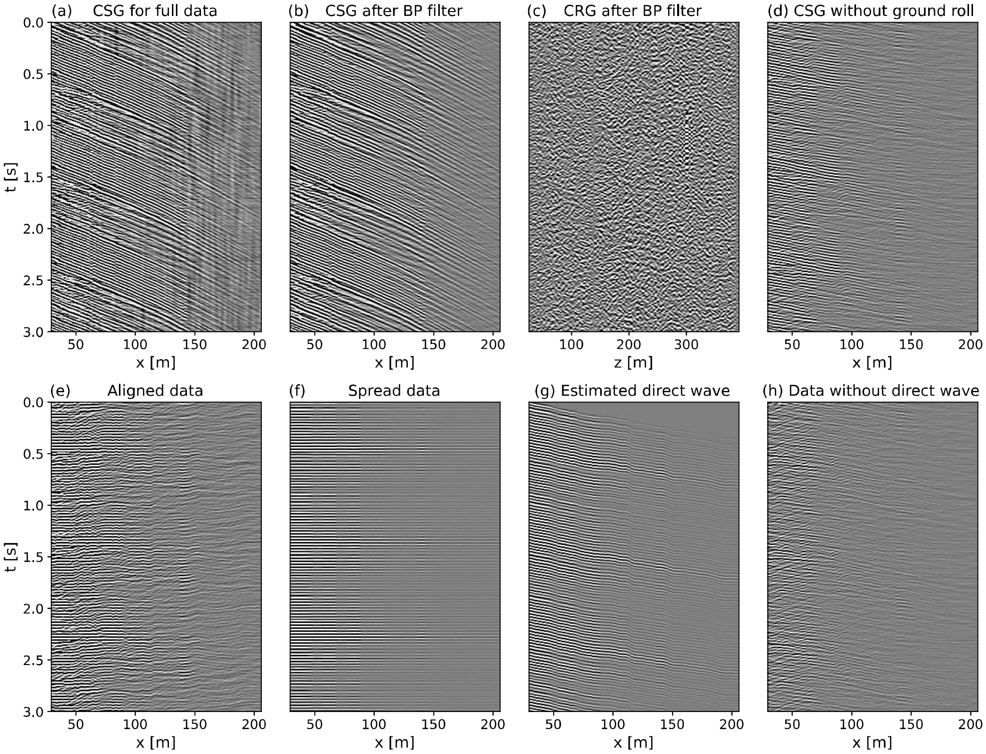

Figure 14. (a) CSG of the full data, (b) CSG after using BP filter, (c) CRG after using BP filter, (d) CSG after without ground roll, (e) aligned wavefield using the optimized time shift, (f) spread wavefield, (g) estimated direct arrival wavefield, (h) wavefield without the direct arrival

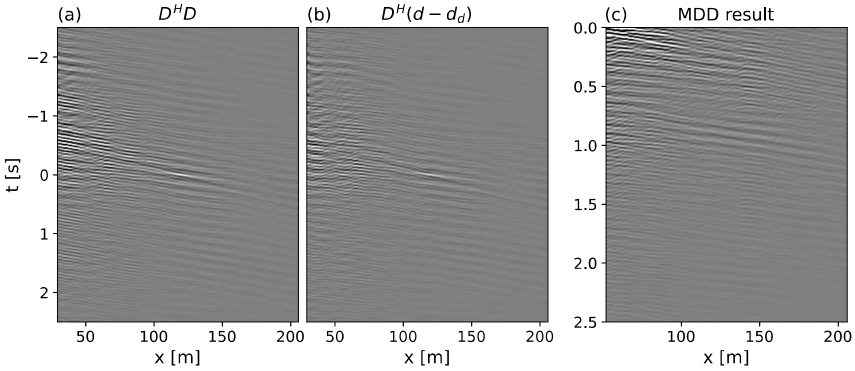

Figure 15. (a) Auto-correlation of the wavefield without ground roll, (b) cross-correlation between the wavefield without ground roll and the wavefield with both the ground roll and direct arrival removed, (c) reconstructed reflection response using MDD.

ful application to a field data set further confirms the robustness, effectiveness, and practicality of this method in field data scenarios. Overall, the proposed method provides a practical and reliable solution for SWD imaging, establishing foundations for future applications in both exploration and real-time subsurface monitoring.

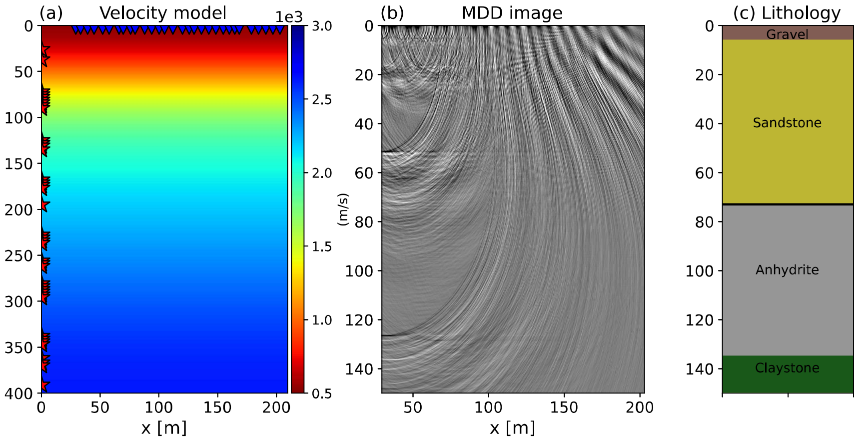

Figure 16. (a) Velocity model used for migration, (b) MDD imaging result, and (c) lithological changes from the drilling report.

Open Research Section

The code supporting the findings of this study will be made available after the paper is published. The model used in the synthetic example is adapted from the open-source SEAM Arid model (Oristaglio, 2015). The field dataset acquired on the KAUST campus will also been made publicly available in accordance with institutional data sharing policies after the paper is published.

Inclusion in Global Research Statement

This research is conducted as part of an academic collaboration based at King Abdullah University of Science and Technology (KAUST), Saudi Arabia. The field dataset used in this study was acquired during a drilling campaign on the KAUST campus, with all necessary permissions and access granted through institutional coordination. No external permits were required for data collection. All contributors who meet the authorship criteria set by AGU Publications are listed as co-authors.

This research aligns with the principles of transparency, fairness, and equitable collaboration as outlined in The TRUST Code. The proposed method aims to support both local and international geophysical communities by promoting accessible, cost-effective and accurate approaches to SWD data processing.

Acknowledgments

This publication is based upon work supported by King Abdullah University of Science and Technology (KAUST) under Award No. RFS-OFP2023-5606. We are grateful to the members of the Deep Imaging Group (DIG) for their support in the data acquisition campaign. We also thank DIG and Seismic Wave Analysis Group (SWAG) for the insightful discussions. AI-based tools (ChatGPT) were used solely for grammar and consistency checking during manuscript preparation, including improving clarity, coherence, and conciseness in the writing process. No AI-generated content was included in the final manuscript.

References

Asgharzadeh, M., Grant, A., Bona, A., & Urosevic, M. (2019). Drill bit noise imaging without pilot trace, a near-surface interferometry example. *Solid Earth*, *10*(4), 1015–1023. Retrieved from `https://se.copernicus.org/articles/10/1015/2019/` doi: 10.5194/se-10-1015-2019

Bakulin, A., Aldawood, A., Silvestrov, I., Hemyari, E., & Poletto, F. (2020). Seismic-while-drilling applications from the first drillcam trial with wireless geophones and instrumented top drive. *The Leading Edge*, *39*(6), 422–429.

Boiero, D., Mahat, S., Bagaini, C., & Ortin, M. (2023). True-amplitude multiple prediction in sparse ocean-bottom acquisitions using a multidimensional deconvolution approach. *84th EAGE Annual Conference and Exhibition*, *2023*(1), 1-5. Retrieved from `https://www.earthdoc.org/content/papers/10.3997/2214-4609.202310695` doi: https://doi.org/10.3997/2214-4609.202310695

Campillo, M., & Paul, A. (2003). Long-range correlations in the diffuse seismic coda. *Science*, *299*(5606), 547-549. doi: 10.1126/science.1078551

Claerbout, J. F. (1968, April). Synthesis of a Layered Medium from its Acoustic Transmission Response. *Geophysics*, *33*(2), 264. doi: 10.1190/1.1439927

de Ridder, S. A. L., & Biondi, B. L. (2013). Daily reservoir-scale subsurface monitoring using ambient seismic noise. *Geophysical Research Letters*, *40*(12), 2969-2974. doi: https://doi.org/10.1002/grl.50594

Galetti, E., Curtis, A., Baptie, B., Jenkins, D., & Nicolson, H. (2017). Transdimensional love-wave tomography of the british isles and shear-velocity structure of the east irish sea basin from ambient-noise interferometry. *Geophysical Journal International*, *208*(1), 36–58.

Goertz, A., Atkinson, B., Thiem, T., & Bergfjord, E. V. (2020). Reservoir imaging-while-drilling with prm arrays. *First Break*, *38*(11), 77–83. Retrieved from `https://doi.org/10.3997/1365-2397.fb2020083` doi: 10.3997/1365-2397.fb2020083

Guy, M. (1961). *Nouvelle methode de controle geologique de forage* (Brevet d'Invention No. 1.584.951). Ministere du Developpement Industriel et Scientifique, Republique Francaise.

Haacke, R., & Poole, G. (2023). Source-side multi-dimensional deconvolution using a downgoing annihilation filter approach. *84th EAGE Annual Conference and Exhibition*, *2023*(1), 1-5. doi: 10.3997/2214-4609.2023628014

Hardage, B. A. (2000). *Vertical seismic profiling: Principles*. Elsevier.

Jardine, S., Lesage, M., & McCann, D. (1990). Estimating tooth wear from roller cone bit vibration. In *Iadc/spe drilling conference.* (IADC/SPE Paper No. 19966)

Katz, L. (1984). *Method and system for seismic continuous bit positioning* (Patent Nos. US 4,460,059). U.S. Patent Office.

Kennedy, J., & Eberhart, R. (1995). Particle swarm optimization. In *Proceedings of ieee international conference on neural networks* (Vol. 4, pp. 1942–1948).

Khaled, O. S., Al-Ateeqi, A. M., James, A. R., & Meehan, R. J. (1996). Seismic-while-drilling in kuwait results and applications. *GeoArabia*, *1*(4), 531–550.

Langenkamp, R. D. (1994). *The illustrated petroleum reference dictionary / edited by robert d. langenkamp.* (4th edition ed.). Tulsa, Oklahoma: PennWell.

Miller, D., Haldorsen, J., & Kostov, C. (1990). *Methods for deconvolution of unknown source signatures from unknown waveform data* (Patent Nos. US 4,922,362). U.S. Patent Office.

Miranda, F., Aleotti, L., Abramo, F., Poletto, F., Craglietto, A., Persoglia, S., & Rocca, F. (1996). Impact of the seismic while drilling technique on exploration wells. *First Break*, *14*(2).

Mordret, A., Rivet, D., Landès, M., & Shapiro, N. M. (2015). Three-dimensional shear velocity anisotropic model of piton de la fournaise volcano (la réunion island) from ambient seismic noise. *Journal of Geophysical Research: Solid Earth*, *120*(1), 406-427. doi: https://doi.org/10.1002/2014JB011654

Naville, C., Serbutoviez, S., Throo, A., Batini, F., Dini, I., & Cecconi, F. (2000).

Drillbit swd reverse walkaway using downhole reference signal. In *Spe/iadc drilling conference.* (SPE Paper No. 65115)

Naville, C., Serbutoviez, S., Throo, A., Vinck, O., & Cecconi, F. (2004). Seismic while drilling (swd) techniques with downhole measurements, introduced by ifp and its partners in 1990-2000. *Oil & Gas Science and Technology*, *59*, 371–403.

Oristaglio, M. (2015). Seam update. *The Leading Edge*, *34*(4), 466-468. doi: 10.1190/tle34040466.1

Picozzi, M., Parolai, S., Bindi, D., & Strollo, A. (2009). Characterization of shallow geology by high-frequency seismic noise tomography. *Geophysical Journal International*, *176*(1), 164–174.

Poletto, F., Bellezza, C., Corubolo, P., Goertz, A., Bergfjord, E. V., & Lindgård, J. E. (2019). Seismic while drilling using a large-aperture ocean bottom array. In *Seg technical program expanded abstracts* (pp. 5320–5324).

Poletto, F., Corubolo, P., & Comelli, P. (2010). Drill-bit seismic interferometry with and without pilot signals. *Geophysical Prospecting*, *58*, 257–265. doi: 10.1111/j.1365-2478.2009.00832.x

Poletto, F., & Dordolo, G. (2002). A new approach to offshore drill-bit rvsp. *Geophysics*, *67*, 1071–1075.

Poletto, F. B., & Miranda, F. (2022). *Seismic while drilling - fundamentals of drill-bit seismic for exploration, 2nd edition.* Elsevier.

Ravasi, M., Selvan, T., & Luiken, N. (2022). Stochastic multi-dimensional deconvolution. *IEEE Transactions on Geoscience and Remote Sensing*, *60*, 1-14. doi: 10.1109/TGRS.2022.3179626

Rector, I., J. W. (1989). *System for reducing drill string multiples in field signals* (Tech. Rep. Nos. 4,862,423). U.S. Patent Office.

Rocca, F., Persoglia, S., Poletto, F., & Craglietto, A. (1990). *Use of drilling noise to generate a reciprocal vsp* (Tech. Rep.). CEE Contract DGXII/TH-0113-87, Final Report of the Project.

Schuster, G. T. (2009). *Seismic interferometry.* Cambridge: Cambridge University Press.

Schuster, G. T. (2014). Seismic interferometry. In *Encyclopedia of exploration geophysics* (pp. Q1-1–Q1-41). Oklahoma, USA: Society of Exploration Geophysicists.

Seeman, B., & Horowicz, L. (1983). Vertical seismic profiling: Separation of upgoing and downgoing acoustic waves in a stratified medium. *GEOPHYSICS*, *48*(5), 555-568. doi: 10.1190/1.1441486

Silvestrov, I., Hemyari, E., Bakulin, A., Luo, Y., Aldawood, A., Poletto, F., … Golikov, P. (2021, November). Processing of seismic-while-drilling data from the drillcam system acquired with wireless geophones, top-drive, and downhole vibrations sensors. *SPE Middle East Oil and Gas Show and Conference*, D031S017R002. doi: 10.2118/204543-MS

Stuart, J. (1989). *Method for determining drill bit wear: European patent application* (European Patent Application No. EP 0 336 477 A1). European Patent Office.

Vasconcelos, I., & Snieder, R. (2008a). Interferometry by deconvolution: part 1 – theory for acoustic waves and numerical examples. *Geophysics*, *73*(3), S115–S128.

Vasconcelos, I., & Snieder, R. (2008b). Interferometry by deconvolution: part 2 – theory for elastic waves and application to drill-bit seismic imaging. *Geophysics*, *73*(3), S129–S141.

Vidal, C. A., & Wapenaar, K. (2014). Passive seismic interferometry by multidimensional deconvolution-decorrelation. *SEG Technical Program Expanded Abstracts*, 2224-2228. doi: 10.1190/segam2014-1208.1

Wang, N., & Ravasi, M. (2023). Upside down Rayleigh-Marchenko imaging: Towards a practical exact redatuming scheme for ocean bottom acquisitions. *Third In-*

ternational Meeting for Applied Geoscience & Energy Expanded Abstracts, 1411-1415.

Wang, N., & Ravasi, M. (2024). Upside-down Rayleigh-Marchenko: a practical redatuming scheme for seabed seismic acquisitions. *Geophysics*, *89*(6), 1-67. doi: 10.1190/geo2023-0743.1

Wapenaar, K., & Fokkema, J. (2006). Green's function representations for seismic interferometry. *Geophysics*, *71*(4), SI33-SI46. doi: 10.1190/1.2213955

Wapenaar, K., van der Neut, J., Ruigrok, E., Draganov, D., Hunziker, J., Slob, E., … Snieder, R. (2011). Seismic interferometry by crosscorrelation and by multidimensional deconvolution: A systematic comparison. *Geophysical Journal International*, *185*(3), 1335–1364.

Weatherby, B. B. (1936). *Method of making sub-surface determinations* (Tech. Rep. Nos. 2,062,151). U.S. Patent Office.

Zhang, Z. d., Alajami, M., & Alkhalifah, T. (2020, 05). Wave-equation dispersion spectrum inversion for near-surface characterization using fibre-optics acquisition. *Geophysical Journal International*, *222*(2), 907-918. doi: 10.1093/gji/ggaa211